Journal of Computational Physics 228 (2009) 3936–3972

Contents lists available at ScienceDirect

Journal of Computational Physics

journal homepage: www.elsevier.com/locate/jcp

On the outflow conditions for spectral solution of the viscous blunt-body problem

Kazem Hejranfar [a,*], Vahid Esfahanian [b], Mehdi Najafi [a]

[a] Aerospace Engineering Department, Sharif University of Technology, Tehran 11365-8639, Iran
[b] Mechanical Engineering Department, University of Tehran, Tehran, Iran

ARTICLE INFO

Article history:
Received 10 September 2007
Received in revised form 6 February 2009
Accepted 9 February 2009
Available online 20 February 2009

Keywords:
Blunt-body
High-speed flows
Subsonic outflow
Spectral methods

ABSTRACT

The purpose of this paper is to study and identify suitable outflow boundary conditions for the numerical simulation of viscous supersonic/hypersonic flow over blunt bodies, governed by the compressible Navier–Stokes equations, with an emphasis motivated primarily by the use of spectral methods without any filtering. The subsonic/supersonic composition of the outflow boundary requires a dual boundary treatment for well-posedness. All compatibility relations, modified to undertake the hyperbolic/parabolic behaviour of the governing equations, are used for the supersonic part of the outflow. Regarding the unknown downstream information in the subsonic region, different subsonic outflow conditions in the sense of the viscous blunt-body problem are examined. A verification procedure is conducted to make out the distinctive effect of each outflow condition on the solution. Detailed comparisons are performed to examine the accuracy and performance of the outflow conditions considered for two model geometries of different surface curvature variations. Numerical simulations indicate a noticeable influence of pressure from subsonic portion to supersonic portion of the boundary layer. It is demonstrated that two approaches for imposing subsonic outflow conditions namely (1) extrapolating all flow variables and (2) extrapolation of pressure along with using proper compatibility relations are more suitable than the others for accurate numerical simulation of viscous high-speed flows over blunt bodies using spectral collocation methods.

1. Introduction

In most branches of engineering and applied mathematics, the numerical solution of a system of partial differential equations in a truncated domain as a part of an unbounded physical domain, is a common challenge. For such problems formulated on an unbounded domain, there are generally many different ways of closing its truncated counterpart and the choice of required artificial boundary conditions is not unique [1–3]. One aspect which has both theoretical and computational importance is the definition and treatment of these conditions. As has been frequently shown theoretically and numerically, the overall accuracy and performance of numerical solutions strongly depend on the proper treatment of boundaries. Exact boundary conditions and accurate boundary treatments allow one to greatly reduce the size of the computational domain while still maintaining accuracy of the solution. Moreover, they may provide a noticeable speedup of convergence rate of the solution [1].

In the study of fluid flow, the boundary conditions of the region of the interest play a significant role. Reflection of spurious waves at the boundaries and distortion of outgoing flow structures are not desired and have to be minimized, mean-

* Corresponding author.
E-mail address: khejran@sharif.edu (K. Hejranfar).

0021-9991/$ - see front matter © 2009 Elsevier Inc. All rights reserved.
doi:10.1016/j.jcp.2009.02.010

while the exact inflow and outflow conditions have to be enforced. The numerical coupling between the inflow and outflow boundaries, which can potentially result in non-physical oscillations in the computational domain, especially when using high-order low dissipative methods, should be taken into account with a depth of care [4–10].

Mathematically, the boundary conditions of a system of equations are subjected to result in a bounded unique boundary dependent solution in order for the problem to be well-posed. The number of physical boundary conditions for the well-posedness requirement for the Euler and Navier–Stokes equations have been derived by Strikwerda [11] and Oliger and Sundstrom [13]. These boundary conditions are provided by some information about the external flow, adjacent to the boundaries, which are commonly known as physical boundary conditions. In some cases, however, no accurate external flow information is available, such as at the subsonic outflow boundary. Hayder and Turkel [12] considered many types of outflow boundary conditions in the calculation of a jet where no boundary data were available. The results were not encouraging and emphasized on the need for more investigation in this area.

Although mathematically only a certain number of boundary conditions are required for the system of Euler and Navier–Stokes equations, depending on the local flow conditions, numerically, it is necessary to specify all the dependent variables there [11]. When using high-order numerical methods, this part requires critical treatments. Even with physically known and mathematically well-posed boundary conditions, some high-order methods have boundary closure problems, like compact finite-difference schemes. The main limiting factor in the application of such high-order schemes is finding stable boundary scheme that preserve their formal accuracy. Their formal accuracy is to one order higher than the boundary condition accuracy [14–16]. The numerical instability in the boundary is usually covered up with filters in these schemes. The stability characteristic of various compact schemes are used to assess the theory of Gustafsson, Kreiss and Sundstrom (G–K–S) [17] for semidiscrete initial boundary value problems in [14,15] and a systematic technique is presented for constructing stable and accurate boundary closures of various orders satisfying the summation-by-parts energy norm. In a further study, Carpenter et al. [18] have proposed various methods including introduction of a simultaneous approximation term (SAT) to obtain asymptotic and G–K–S stable boundary schemes. Beside these classes of high-order schemes, spectral methods do not suffer from such issues because of global character of their discretization and this makes them a proper test for all sorts of boundary conditions. But, they are well-known as being very sensitive to boundary treatment and only in simple problems they are rather easy to cope with [5–7].

Along an artificial boundary, some dependent variables left unspecified by the physical boundary conditions. To complete the specification of the variables, solving a set of compatibility equations for high-order methods and usually a simple extrapolation of the dependent variables from interior points to the boundary for low-order methods are recommended in the literature. In the case of a subsonic outflow boundary, such as the outflow condition of the viscous blunt-body problem, we need one physical and three numerical boundary conditions [19–21]. The physical boundary condition can be satisfied by prescribing one dependent variable, for instance the pressure. Then numerical conditions are satisfied by the compatibility equations corresponding to the outgoing characteristics or extrapolating the velocity components and the density from the interior points. Artificial boundary conditions have been formulated for the nonlinear Euler and Navier–Stokes equations extensively (e.g. see Thompson [19], Poinsot and Lele [20], Hirsch [21], Dutt [22], Hagstrom and Hariharan [23], Hedstrom [24] and Nordström and Svard [25]). But there are few articles on the treatments with the missing information at the boundary [3].

With the increase of computational power, accurate solutions to the Navier–Stokes equations for compressible boundary layer flows became feasible and overviews can be found in [26–31]. This is especially important where experimental approaches have encountered enormous difficulties in obtaining accurate flow quantities. The prerequisite of such computations is highly accurate solutions. The viscous blunt-body problem has been studied through several high-order methods, during last decades for the weak, moderate and strong interactions of the boundary layer with the outer stream. For this class of viscous flows, a very accurate steady solution is usually required before an unsteady analysis could be attempted. The spectral solution of the steady problem is presented by Kopriva [32–34]. One of the most interesting properties of spectral methods is their exponential rate of convergence and high-order accuracy even on coarse grids, which made them the method of the choice for highly accurate computations.

As a popular issue with the viscous blunt-body problem, the region where the boundary layer meets the outflow and the flow is subsonic, needs special treatment due to incoming downstream information which is generally unknown. This made Kopriva's results to suffer from lack of accuracy due to the missing information from the downstream (mainly the correct pressure distribution) [32]. In the case of hypersonic flow over a cylinder, he used a fixed pressure distribution along the subsonic outflow obtained from the inviscid solution of the same problem [32,34]. Consequently, his approach brought predictions of body surface quantities with errors of 35% in the pressure coefficient and 29% in the heating rate near the outflow region. For a hyperbolic cone geometry, he used a viscous shock layer (VSL) solution to obtain that constant pressure distribution across the subsonic outflow with a better accuracy. Although the results of Kopriva [32] well agreed by low-order finite-difference VSL code of [35], they are not self-sustained and not essentially accurate in the sense of high-order computations.

Whereas the mathematical requirement for well-posedness has found a general acceptance (see Nordström and Svord [25]), there is still no general method to define the physical boundary conditions if the required external information is lacking. There are several methods to tackle with this unknown information. Using boundary layer theory assumptions, employing inviscid calculations, using fringe and absorbing-layer type methods, extrapolation methods and so on are the well-known remedies in the literature. Colonius [2] has reviewed a variety of accurate techniques for a linearized model near

the boundary and ad hoc ones for nonlinear case, like absorbing layers and fringe methods. In his detailed study, he revealed that many of these methods require several tunable parameters and blending functions that have only been optimized by trial and error; thus they are specific to the problem.

Gustafsson and Nordström [36] showed that a well-posed problem is obtained at the subsonic outflow boundary, if one extrapolates all the variables inside the boundary layer. Generally speaking, the extrapolation methods can be used for the specification of the numerical boundary conditions, and where there is a dominant flow direction, they can serve as an alternative physical boundary condition, in case that no external information is available. Such procedures at subsonic artificial outflow boundaries can be used even for time dependent problems if sufficiently large transverse gradients are present in the flow field [37]. It is shown in [37] that if the subsonic part of the outflow is contained completely within the boundary layer, the extrapolation methods give accurate results.

The use of derivative boundary conditions at artificial outflow with errors in the boundary data of order one has been investigated by Nordström [3]. In his work, both the problem when the artificial outflow boundary is located in essentially uniform flow and the situation when the artificial outflow boundary is located in a flow field with large gradients were discussed. For the case of subsonic outflow, he stated that unlike the supersonic outflow, accurate solutions can be obtained by using derivative boundary conditions if and only if large transversal gradients are present in the flow field. In this case, he showed the reliability of extrapolation methods even in the subsonic outflow.

Extrapolation boundary conditions tie with derivative conditions in the continuous region. Two kinds of extrapolations can be assumed: flux extrapolation and variable extrapolation. For the supersonic outflow it was shown in [38] that there is a loss of accuracy in long time integration for continuous linearized Navier–Stokes equations when using flux extrapolation (unlike variable extrapolation) and they are not appropriate for long time integration.

In this paper, we are on to study and examine some different outflow boundary conditions in simulating the viscous supersonic/hypersonic flow over blunt bodies by means of spectral collocation methods to identify appropriate ones in obtaining accurate solutions in the whole flow field. The dual composition of the outflow boundary necessitates individual treatments in each part. For the supersonic portion, the proper compatibility equations with viscous considerations are used. At the subsonic portion, where a flow condition from the unknown downstream is required, miscellaneous techniques are proposed. These include (1) removing streamwise pressure gradient partly or completely, (2) sublayer approximation, (3) utilizing inviscid solution of the same problem, (4) boundary non-reflectivity condition, (5) extrapolation of all primitive variables and (6) extrapolating the pressure along with using proper compatibility relations. A verification procedure is suggested to investigate the accuracy, behaviour and performance of each of the above outflow techniques through shrinking/extending body geometry. As the paper is organized to be self contained, a quick look on the governing equations, boundary conditions and numerical method are given. After that, the above techniques in resolving subsonic outflow boundary with their advantages and disadvantages are studied in detail. A hypersonic viscous flow of Mach 5.73 over a circular cylinder is considered as the model problem. Experimental and numerical comparisons are made to investigate and suggest the most proper ones, in order to obtain stable, convergent, self-stand and the most accurate solution for the model problem in case of either adiabatic or isothermal surface condition. Then, a hypersonic viscous flow at Mach 15 over a parabola is computed to examine the accuracy and performance of the proposed boundary conditions at the subsonic outflow on the solution. Finally, we sum up and draw conclusions.

2. Problem definition

The viscous supersonic flow over a blunt-body at zero angle of attack is considered as the model problem (Fig. 1). The shock-fitting technique is used to treat the strong bow shock. The symmetry facilitates the solution as we need to solve only the upper-half of the flow field.

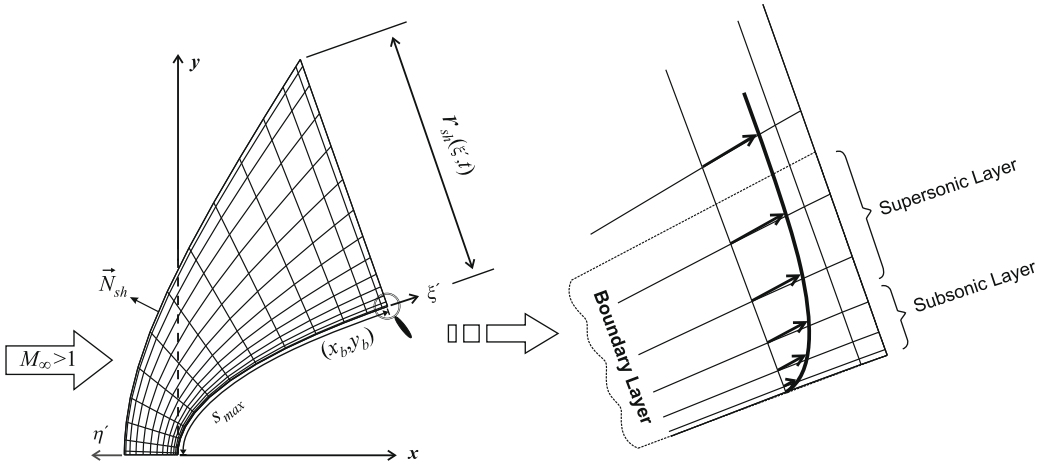

Fig. 1. Schematic of the body fitted grid over a blunt-body at high-speed flows and the dual composition of the outflow boundary.

Here, the compressible Navier–Stokes equations in the primitive and non-conservative form are the governing equations for the two dimensional ($\alpha = 0$) and axisymmetric ($\alpha = 1$) geometries. In the non-dimensional vector form, they can be written as

$$\frac{\partial Q}{\partial t} + A\frac{\partial Q}{\partial x} + B\frac{\partial Q}{\partial y} + \alpha\frac{v}{y}H = \frac{\sqrt{\gamma}M_\infty}{Re_\infty}F_v, \tag{1}$$

where

$$Q = \begin{bmatrix}\rho\\ u\\ v\\ p\end{bmatrix},\quad A = \begin{bmatrix}u & \rho & 0 & 0\\ 0 & u & 0 & \frac{1}{\rho}\\ 0 & 0 & u & 0\\ 0 & \gamma p & 0 & u\end{bmatrix},\quad B = \begin{bmatrix}v & 0 & \rho & 0\\ 0 & v & 0 & 0\\ 0 & 0 & v & \frac{1}{\rho}\\ 0 & 0 & \gamma p & v\end{bmatrix},\quad H = \begin{bmatrix}\rho\\ 0\\ 0\\ \gamma p\end{bmatrix},\quad F_v = \begin{bmatrix}0\\ \sigma_x/\rho\\ \sigma_y/\rho\\ \frac{\gamma}{Pr}\nabla\cdot(k\nabla T) + (\gamma-1)\Phi\end{bmatrix}, \tag{2}$$

and

$$\begin{aligned}
\sigma_x &= \frac{\partial}{\partial x}\left\{\frac{2}{3}\mu\left(2\frac{\partial u}{\partial x} - \frac{\partial v}{\partial y} - \frac{\alpha v}{y}\right)\right\} + \left(\frac{\partial}{\partial y} + \frac{\alpha}{y}\right)\left\{\mu\left(\frac{\partial v}{\partial x} + \frac{\partial u}{\partial y}\right)\right\},\\
\sigma_y &= \frac{\partial}{\partial x}\left\{\mu\left(\frac{\partial v}{\partial x} + \frac{\partial u}{\partial y}\right)\right\} + \frac{\partial}{\partial y}\left\{\frac{2}{3}\mu\left(2\frac{\partial v}{\partial y} - \frac{\partial u}{\partial x} - \frac{\alpha v}{y}\right)\right\} + \frac{\alpha}{y}\left\{2\mu\left(\frac{\partial v}{\partial y} - \frac{v}{y}\right)\right\},\\
\sigma_{xy} &= \mu\left(\frac{\partial v}{\partial x} + \frac{\partial u}{\partial y}\right),\\
\nabla\cdot(k\nabla T) &= \frac{\partial}{\partial x}\left(k\frac{\partial T}{\partial x}\right) + \left(\frac{\partial}{\partial y} + \frac{\alpha}{y}\right)\left(k\frac{\partial T}{\partial y}\right),\\
\Phi &= \mu\left(\frac{\partial v}{\partial x} + \frac{\partial u}{\partial y}\right)^2 + \frac{4}{3}\mu\left(\left(\frac{\partial u}{\partial x}\right)^2 + \left(\frac{\partial v}{\partial y}\right)^2 + \frac{\alpha v}{y}\left(\frac{v}{y} - \left(\frac{\partial u}{\partial x} + \frac{\partial v}{\partial y}\right)\right)\right) - \frac{\partial u}{\partial x}\frac{\partial v}{\partial y}.
\end{aligned} \tag{3}$$

The coordinate system is non-dimensionalized with a reference length (nose radius, R_{nose}). The density, pressure and temperature which are denoted by ρ, p and T, are scaled with their freestream values. The velocities u and v are scaled with the freestream isothermic speed of sound, $\sqrt{p_\infty/\rho_\infty}$, while its inverse multiplied by the nose radius is used for non-dimensionalizing the time.

The equations are well set by the freestream Mach, Reynolds and Prandtl numbers (which are denoted by M_∞, Re_∞ and Pr, respectively). Note that the Reynolds number is based on the reference length. The equation of state for the air as a perfect gas ($p = \rho T$) and the Sutherlands law for the viscosity coefficient (which is scaled by its freestream value)

$$\mu = T^{\frac{3}{2}}\frac{1+c}{T+c},\quad c = \frac{110.33\ (\text{K})}{T_\infty} \tag{4}$$

are considered to close the system of equations [39]. The Prandtl number is assumed to be a constant value so the dimensionless thermal conductivity coefficient is the same as the dimensionless viscous coefficient ($k = \mu$). The specific heats ratio, γ, is also assumed to be a constant value.

For axisymmetric formulation, along the symmetry axis where a singularity appears, the L'Hopital's rule is used in order to accurately evaluate the inviscid source terms and the viscous fluxes [32].

The governing equations are expressed in terms of general curvilinear coordinates (ξ', η', t) along body fitted grid lines and are solved on a standard square computational domain (ξ, η, t). The bow shock is treated as a computational boundary where the shock movement is solved as a part of the solution. Consequently, the grid lines of constant η' are unsteady due to shock movements, but the grid lines of constant ξ' are fixed during calculations.

3. Boundary conditions

The flow field is exposed to four boundaries: the bow shock at the top, the symmetry axis at the left, the body surface at the bottom and the outflow at the right (see Fig. 1). For each boundary, a set of boundary conditions is provided by many authors [13,19–21] that insures the well-posedness of the governing equation. These conditions are of both Dirichlet and Neumann types. The imposition of each type is straight forward in spectral collocation methods, which is described extensively in [5,6] and suited specially for this problem in [7–10,32].

3.1. Shock boundary

In a transition of a viscous gas through a shock wave over a blunt-body, a thickness of the transitional region, δ_s, can be predicted using an estimate by Moretti and Salas [40]:

$$\delta_s \approx \frac{8}{3Re_\infty}\frac{\gamma}{\gamma+1}\frac{M_\infty^2 - 1}{1 + \gamma M_\infty^2 - M_\infty\sqrt{2(\gamma+1)(1 + M_\infty^2(\gamma-1)/2)}}, \tag{5}$$

where δ_s is scaled with the nose radius of curvature of the blunt-body and the Reynolds number is based on this reference value. In Fig. 2, a plot of δ_s against Reynolds and Mach numbers is presented. Within a numerical computation of a viscous flow with shocks, if the shock thickness becomes a negligible value compared with the minimum grid spacing near the shock, this transition cannot be distinguished from a sharp discontinuity. In this case, considering a curve as the shock profile is a good estimate.

In this study, the shock-fitting method is used to obtain the shock position, as it is a computational boundary, and post-shock flow variables accurately. This is done by means of the Rankine–Hugoniot relations and the compatibility equation corresponding to the characteristic variable carrying information from inside toward the shock, as in [8–10,32,34,41]. The initial shock profile is approximated by the correlation of Billig [42]. The shock profile is updated after each time step. For a steady solution, it will reach a final position.

3.2. Wall boundary

The no-slip boundary condition is used for the velocity and the adiabatic or isothermal condition is assumed for the temperature at the body surface as the flow is within the continuum regime:

$$u = v = 0, \quad T = T_w \quad \text{or} \quad \frac{\partial T}{\partial n} = 0, \tag{6}$$

where T_w is a fixed temperature value for the body surface and n denotes the body normal direction. There are two ways to compute the wall pressure and density. In the first method, the wall pressure is obtained using the compatibility equation corresponding to the incoming (reflected) acoustic wave from the body surface as theoretically recommended by many authors (like, Thompson [19] and Poinsot and Lele [20] and Hirsch [21]). This procedure has been confirmed numerically to be well suited for wall pressure calculations, using spectral collocation methods for inviscid and viscous flows [7–10,32–34]. This compatibility equation is

$$[0, \rho a N_{bx}, \rho a N_{by}, -1] \cdot \left[\frac{\partial Q}{\partial t} + A\frac{\partial Q}{\partial x} + B\frac{\partial Q}{\partial y} + \alpha\frac{v}{y}H = \frac{\sqrt{\gamma}M_\infty}{Re_\infty}F_v\right], \tag{7}$$

where N_{bx} and N_{by} are the Cartesian components of the body normal direction and a is the local speed of sound. In case of adiabatic body surface condition, the zero heat flux across the body is implemented implicitly within Eq. (7) when computing viscous fluxes. This equation includes the time derivative of the velocities and pressure together. For no-slip body surface, the time derivative of the velocity components are zero and thus, the compatibility Eq. (7) just represents the time derivative of the pressure at the wall. Therefore, the wall pressure is evaluated accurately with this compatibility equation, where generation of no spurious waves from the body surface is totally guaranteed.

For the isothermal body surface, the density is obtained directly from the equation of state by the computed wall pressure and the given wall temperature. For the adiabatic case, there are three ways to evaluate the density at the wall:

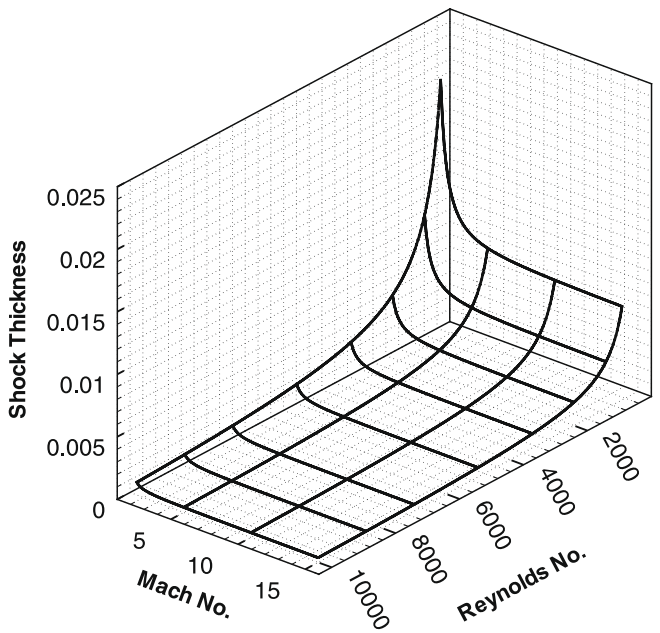

Fig. 2. Viscous shock thickness for a range of Reynolds and Mach numbers.

(1) *The direct use of the equation of state*: Having known the wall pressure and obtaining the wall temperature from zero heat flux at the wall, the equation of state gives the density directly.
(2) *The indirect use of the equation of state*: The zero heat flux across the body surface can give a relation between the pressure gradient normal to the body and the density gradient in the same direction, i.e.:

$$\frac{1}{\rho}\frac{\partial \rho}{\partial n} = \frac{1}{p}\frac{\partial p}{\partial n}. \tag{8}$$

Again, n is the boundary-normal direction. Having known the pressure distribution, the density can be obtained easily. Then, the temperature is evaluated using the equation of state.
(3) *Using the compatibility equation corresponding to the propagation of the entropy wave*: In this way, the temperature condition is imposed implicitly and the following compatibility equation, which corresponds to the propagation of the entropy wave, is integrated along with the compatibility Eq. (7) to obtain the density at the wall

$$[a^2, 0, 0, -1] \cdot \left[\frac{\partial Q}{\partial t} + A\frac{\partial Q}{\partial x} + B\frac{\partial Q}{\partial y} + \alpha\frac{v}{y}H = \frac{\sqrt{\gamma}M_\infty}{Re_\infty}F_v\right]. \tag{9}$$

Then, using the equation of state, the adiabatic temperature can be easily obtained.

The second method for computation of the wall pressure begins with determination of the density directly from the continuity equation. Having the wall temperature either given at the isothermal wall or calculated from zero heat flux of adiabatic surface, the wall pressure is evaluated from the equation of state [43,44]. This method has also put into work and carried out a stable solution in the present study, unlike Kopriva [32]. Although computing the wall pressure from the compatibility Eq. (7) seems to present a complete description of the boundary behaviour than the second one, as it comes from the physical fact of wave reflections from the body surface, the second method, which takes advantage of no-slip condition, gives the same results. Consequently, the first method is applicable to both the inviscid and viscous problems, while the second method is only apt for the viscous ones.

3.3. Symmetry axis boundary

The flow conditions at the left boundary are geometrically and physically in symmetry along its normal direction. The boundary conditions at this boundary as observed in [7–10,41] to present a well-posed solution and consistent with low dissipative features of the spectral methods are:

$$v = 0, \quad \frac{\partial \rho}{\partial y} = 0, \quad \frac{\partial u}{\partial y} = 0, \quad \frac{\partial p}{\partial y} = 0. \tag{10}$$

3.4. Outflow boundary

At the outflow boundary, unlike the inviscid case [7–9], the conditions are more sophisticated for the viscous case [10]. Sufficiently far from the nose region in the blunt-body problem, the flow remains supersonic after crossing the shock and the presence of the boundary layer divides the outflow boundary into supersonic and subsonic parts (see Fig. 1). At both parts, the parabolic behaviour of the governing equations requires the normal heat flux and the tangential stresses have zero spatial gradients with respect to the boundary-normal direction n, following the theoretical work of [11,13,22], i.e.

$$\frac{\partial \sigma_{xy}}{\partial n} = 0, \quad \frac{\partial}{\partial n}\left(k\frac{\partial T}{\partial n}\right) = 0, \tag{11}$$

which are imposed implicitly while evaluating the viscous fluxes, as in [10,32]. Although from numerical experiences, we observed that fulfilling the number of physical boundary conditions according to the theory of hyperbolic system of equations (e.g. Euler equations) is sufficient at the outflow, the viscous conditions for the incompletely-parabolic Navier–Stokes equations are added implicitly and result only in very small differences. This can be understood from the fact that in the present application, the viscous effects are restricted to the small region near the wall.

3.4.1. Supersonic outflow boundary

At the supersonic part of the outflow, all four characteristic waves leave the computational domain; therefore, there is no need for any explicit condition for the hyperbolic behaviour of the governing equations. For this boundary, all compatibility relations or the governing equations along with implicit implementation of conditions (11) are solved to ensure well-posedness of the solution.

3.4.2. Subsonic outflow boundary

In the subsonic portion of the outflow, the presence of streamwise pressure gradients admits upstream influences. Considering the characteristic analysis of [19–21], beside the parabolic behaviour of the governing equations, in the subsonic

portion of the outflow, the upstream effects should be taken into account in order to meet a well-posed set of equations. This effect is accomplished by the slow acoustic wave entering inside from the outside. The proper choice of downstream condition to include with the governing equations, which is commonly accepted for the subsonic outflow, is the pressure distribution at the outflow to be specified. As stated earlier, while the mathematical requirement for well-posedness has found a general acceptance, there is still no general method to specify the missing downstream pressure distribution at the subsonic outflow boundary.

There are some methods commonly used in the literature to overcome this difficulty. Here, we study and examine some different outflow conditions that do not require any trial and error justifications to resolve the missing downstream information in simulating the viscous supersonic/hypersonic flows over blunt bodies and later will investigate the resulting solutions thoroughly.

(1) *Removing the source of upstream influence partly or completely*: The obvious and simplest approximation is to drop the streamwise pressure gradient in this region, which will be referred to as **BC-1**. Although this has a desirable effect on the convergence from improper initial conditions, the inaccuracies in the solution near the outflow region are the obvious outcome. Based on a hyperbolicity analysis of the partial differential equations, the governing equations in the subsonic layer is forced to remain hyperbolic maintaining a part of pressure gradient. Following the work of Vigneron et al. [45], this is achieved by multiplying the streamwise pressure gradient term in the streamwise momentum equation by a weighting function, $\bar{\omega}$, $(0 \leqslant \bar{\omega} \leqslant 1)$, in order to omit the part responsible for the elliptic behaviour (**BC-1-p**):

$$\bar{\omega} = \min\left(\frac{\gamma M_\xi^2}{1+(\gamma-1)M_\xi^2}, 1\right), \tag{12}$$

where the streamwise Mach number, M_ξ, is defined as:

$$M_\xi = \frac{u\xi_x + v\xi_y}{a\sqrt{\xi_x^2+\xi_y^2}}. \tag{13}$$

(2) *Using the assumptions of the Boundary Layer theory, sublayer approximation*: In the development of the classical boundary layer equations, it is assumed that the normal variation of the pressure is negligible. In this case, the streamwise pressure gradient term from the closest supersonic point to the body is used as a fixed distribution within the governing equations for the whole subsonic layer. Then, the resulting governing equations are solved accordingly (**BC-2**). This technique is known as sublayer approximation [46–48]. Another approximation can be made in the same sense, using the pressure value of that point itself, which faces the governing equations to a new boundary condition and consequently to a new problem, each time the pressure at the supersonic point or the point itself changes. Therefore, the solution is quite based on a suitable initial condition of the numerical simulation, and the rate of convergence is not a satisfactory one. Therefore, in this study the former will be considered only.

(3) *Using the results from inviscid calculations*: In this case, the pressure value of the corner point at the intersection of the outflow and the body from an inviscid solution of the same problem, is considered as a constant pressure distribution for the subsonic outflow (**BC-3**), as used by Kopriva [32]. The first note is that the variation of the pressure along the subsonic layer is neglected. If the numerical simulation does not start with a quite accurate initial condition, this approximation results in an oscillating behaviour near the outflow, because the fixed pressure distribution does not allow the boundary layer to reach to its true thickness. Additionally, as reported by Kopriva [32], the solution becomes erroneous near the subsonic layer of the outflow; in his calculations there was a least 35% of error in the surface pressure coefficient.

(4) *Direct imposition of boundary non-reflectivity*: By removing the wave reflectivity of the boundary, the need for downstream information is totally eliminated, and a stable solution is attained. There are plenty of works in the field of design and application of non-reflective boundary conditions. Although reflection of the outgoing waves through subsonic boundary is a reasonable physical expectance, in some flow field analysis involved with the manual generation and elimination of waves, the non-reflectivity is quite welcome. In this study, we propose and investigate this kind of boundary condition as

$$\frac{\partial p}{\partial \xi} - \rho a\left(\xi_x\frac{\partial u}{\partial \xi} + \xi_y\frac{\partial v}{\partial \xi}\right) = 0, \tag{14}$$

where the streamwise pressure gradient is replaced in the governing equations from the above and they are solved accordingly (**BC-4**).

(5) *Extrapolation of all primitive variables*: As the subsonic part of the outflow is contained completely within the boundary layer, which subjects the flow field to large normal gradients, the extrapolation of all primitive variables are expected to give accurate results [3,37]. In their early use, they were quite successful in conventional low-order finite-difference algorithms. With their legendary formulation, they belong to derivative boundary condition or Neumann type. Here, the following conditions are proposed as the subsonic outflow conditions (**BC-5**):

$$\frac{\partial^2 \rho}{\partial n^2} = 0, \frac{\partial^2 u}{\partial n^2} = 0, \quad \frac{\partial^2 v}{\partial n^2} = 0, \frac{\partial^2 p}{\partial n^2} = 0, \tag{15}$$

where, n is the boundary-normal direction. From the above relations, the primitive variables are calculated globally using the spectral differentiation formula [10]. The temperature is then obtained from the equation of state. Our numerical experiments reveal that if the temperature is used instead of density in the above conditions, the numerical solution may become unstable for improper initial conditions.

(6) *Using extrapolated streamwise pressure*: The use of compatibility relations in this region seems to provide a better approach as they have theoretical approval based on characteristic analysis [19–21]. This inspires the use of second-order or higher extrapolation in obtaining the missing pressure value and using the three compatibility relations corresponding to the outgoing characteristic waves (**BC-6**). In this fashion, the pressure is obtained using

$$\frac{\partial^j p}{\partial n^j} = 0, \tag{16}$$

where n is the boundary-normal direction as before, and j is the order of extrapolation. Here, $j = 2$ is used to be comparable with **BC-5**.

4. Verification procedure

While theoretical tools such as characteristic analysis, Laplace transforms and energy techniques are the most reliable approaches in the sense of defining and analyzing boundary conditions, in practical computations, there is plenty of analytical and empirical knowledge of each boundary type and their importance cannot be overstated. In some cases, theoretical tools are rather difficult or limited to gain some insight to the behaviour of boundary conditions. Sometimes, the boundary conditions are indirectly verified through comparison of the simulation results to available analytical results. In addition, the mathematical theory of the numerical solution of partial differential equations brings some verification rules, which results from the both approaches comply with, e.g. convergence and consistency requirements of the final solution. Since the theoretical tools are quite difficult to tackle with for the problem considered here and there is no analytical solution available for it, the verification is performed numerically.

While high-order compact finite-difference schemes suffer from instability near the boundaries and usually are accompanied with filters, the spectral discretizations, which treat internal and boundary points with an identical formulation, are excellent test methods of alternative conditions for artificial boundaries. In addition, for smooth enough problems they have a competing convergence rate (with minimum resources consumption) to its similar-order finite-differences. As the compressible Navier–Stokes equations are solved just behind the bow shock, the solution we are looking for is analytic within the truncated physical domain. Therefore, we expect exponential decay of error with increase in the grid points and decrease in the domain size [5,6]. Therefore, one can use the points inside the computational domain as the "benchmark" values of the boundary for the smaller domain to examine the accuracy of the implemented conditions at artificial boundaries. This provides adequate evidence regarding a so-called "benchmark" solution for the points located inside the computational domain and on the boundaries with exact conditions implemented, and consequently usability of such a solution for verification purposes [50]. In this study, for each of the mentioned boundary conditions for the subsonic outflow, a set of verification steps can be defined to fulfill the distinctive role of the missing downstream information.

The first verification step is checking the ability to provide a unique convergent solution. The second step emanates from the fact that the main cause of the flow field formation is the physical existence of the body. Therefore, shrinking/extending the body geometry provides a set of comparison check marks to verify the correctness of the converged solution at the artificial outflow boundary (Fig. 3). The body geometry should be extended with special care that flow separation is avoided. In that manner, the flow variables are expected to follow similar trends near the outflow. The coincidence of the flow properties between the points at the outflow and the points at the same location within the extended field is taken as a further verification. The desired stations for the model problem where the comparisons are made, are depicted in Fig. 3. Moreover, the comparison with previous researchers' validated computational or experimental data provides the final check. These steps are considered in this study to identify the accuracy and performance of each outflow boundary conditions proposed in simulating supersonic/hypersonic viscous flows over blunt bodies using spectral collocation methods.

5. Spatial and temporal discretization

The physical region in Fig. 1, is mapped to the square $[-1,1]^2$, like the previous works [10,32], using the following procedure. First, the computational space (ξ_j, η_j), are built from the nodes of a proper Gauss quadrature formula, which is the corner stone of spectral collocation techniques. Given a grid size of $(N_\xi \times N_\eta)$, a set of points is created. While mapping (ξ_j, η_j) domain to the unit square domain (ξ'_j, η'_j), in order to resolve the steep gradients near the body surface due to the presence of the boundary layer, a hyperbolic tangent stretching is used in the direction corresponding to the wall-normal direction as follows:

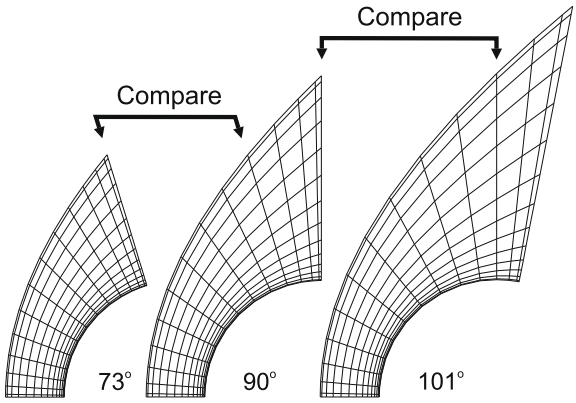

Fig. 3. Schematic shrinked/extended body geometry and stations where comparisons are made for the model problem, a benchmark for verification of the artificial outflow boundary.

$$\xi' = \frac{\xi+1}{2}, \quad \eta' = \frac{1-\tanh(\sigma)}{1-\tanh(\sigma\frac{\eta+1}{2})}\frac{\eta+1}{2}, \tag{17}$$

where σ, is the stretching parameter. Having known the physical distance between the body and the shock wave, $r_{sh}(\xi', t)$, and the maximum value of the body surface parameter, s_{max}, a linear transformation from (ξ', η', t) to the body coordinates (s, r, t) can be defined as

$$s = s_{max}\xi', \quad r = r_{sh}(\xi', t)\eta'. \tag{18}$$

Finally, the intermediate space (s, r, t) is transformed to the physical space (x, y, t), by

$$x = x_b(s) + r(\hat{e}_\eta \cdot \hat{e}_x), \quad y = y_b(s) + r(\hat{e}_\eta \cdot \hat{e}_y), \tag{19}$$

where $\hat{e}_x, \hat{e}_y$ and $\hat{e}_\eta$ are the unit vectors in each subscripted direction.

In the present article, we are concerned with the use of spectral collocation schemes where a function $u(\xi, \eta, t)$ is approximated by a finite combination of orthogonal basis functions defined on the interval $[-1, 1]$ as

$$u(\xi, \eta, t) = \sum_{i=0}^{N_\xi}\sum_{j=0}^{N_\eta} a_{ij}(t)\phi_i(\xi)\phi_j(\eta), \tag{20}$$

where $\phi_k(\cdot)$ stands for the base function of order k. The differentiation in any arbitrary spatial direction, say ξ, can be represented as

$$\frac{\partial}{\partial\xi}u(\xi, \eta, t) = \sum_{i=0}^{N_\xi}\sum_{j=0}^{N_\eta} a_{ij}(t)\phi_i'(\xi)\phi_j(\eta) = \sum_{i=0}^{N_\xi}\sum_{j=0}^{N_\eta} b_{ij}(t)\phi_i(\xi)\phi_j(\eta), \tag{21}$$

and when employing the relation between the coefficients of the function at some collocation points a_{ij}, and its derivative over the same points b_{ij}, it can be interpreted with the physical variables in the form of differentiation matrices as

$$\frac{\partial}{\partial\xi}u_{ij}(\xi, \eta, t) = \sum_{k=0}^{N_\xi} d_{ik}^{\xi}u_{kj}(\xi, \eta, t), \tag{22}$$

and the coefficients d_{ik}^{ξ} are the elements of the differentiation matrix in ξ direction (for detail see [5,6]). It should be noted that with this unique formulation for derivatives at all grid points, there is no place of apprehension about the boundary points. Since the boundary treatment and interior schemes are the same, no instability affects the global accuracy of numerical method. In this study, we choose Gauss–Lobatto quadrature points and Chebyshev polynomials as the basis functions.

Having replaced the derivatives within the governing equations and the boundary conditions with appropriate algebraic expressions, a system of ordinary differential equations in time will be resulted. Here, the time integration is accomplished by means of the fourth-order explicit Runge–Kutta method without any filtering or post-processing procedure. The temporal resolution is controlled by the inviscid CFL number which reflects the stability of the integration as

$$\mathrm{CFL} = \max\left(|U| + a\sqrt{\xi_x^2 + \xi_y^2}, |V| + a\sqrt{\eta_x^2 + \eta_y^2}\right)\frac{\Delta t}{\min(\Delta\xi, \Delta\eta)}, \tag{23}$$

where $U = \xi_t + \xi_x u + \xi_y v$ and $V = \eta_t + \eta_x u + \eta_y v$ are the contra-variant velocity components.

6. Numerical results and discussion

In this section, we consider some of the test cases to examine the accuracy and performance of the proposed outflow boundary conditions in computing supersonic/hypersonic viscous flows over blunt bodies using spectral methods. A high-speed viscous flow of Mach 5.73 over a cylinder is considered as the first model problem. The verification procedure is performed for this model to demonstrate the suitable outflow boundary conditions regarding accuracy and convergence rate for steady state solution. Hypersonic viscous flow of Mach 15 over a parabola is also computed to further investigate the effects of these boundary conditions on the solution. The flow conditions for these model problems are considered such that other numerical/experimental results exist for the validation (see Tables 1 and 2). The grid sizes for the test cases are such that the shock thickness is lower than 0.2% of nose radius which is quite small in comparison with the minimum grid sizes used and the shock is assumed as a sharp discontinuity. Note that the obtained results are the steady state solution of the unsteady compressible Navier–Stokes equations for the air as an ideal gas with specific heat ratio $\gamma = 1.4$ in the absence of any chemical reactions over the model geometries, where the solution is converged to machine precision.

The flow variables such as pressure, temperature and Mach number across the outflow boundary and also body surface quantities are studied for each of the mentioned outflow conditions. The body surface quantities investigated in this study are the pressure coefficient,

$$C_p = \frac{2}{\gamma}\left(\frac{p_{\text{wall}} - 1}{M_\infty^2}\right) \tag{24}$$

the skin friction coefficient,

$$C_f = \frac{2}{\sqrt{\gamma} M_\infty Re_\infty} |\vec{\omega}|_{\text{wall}}, \tag{25}$$

where $|\vec{\omega}|_{\text{wall}} = |\nabla \times \vec{V}|_{\eta'=0}$ is the magnitude of vorticity vector at the wall, the dimensional heat transfer,

$$Q = -\left(\frac{k_\infty T_\infty}{R_{\text{nose}}}\right)(k\vec{\nabla}T \cdot \vec{N}_b)_{\text{wall}}, \tag{26}$$

and the recovery factor,

$$\text{Recovery Factor} = \frac{2}{\gamma - 1}\left(\frac{T_{\text{wall}} - 1}{M_\infty^2}\right). \tag{27}$$

6.1. Cylinder at Mach 5.73

A right circular cylinder of radius $R_{\text{nose}} = 6.1468$ mm is considered due to its simple geometry and existence of some experimental data for the validation, and with flow conditions of Table 1. A (15×15) grid size with the stretching factor of $\sigma = 0.75$ in the wall-normal direction is used for this geometry (Fig. 4). The time integration is progressed using CFL $= 1.2$ to reach steady state. A convergent solution is obtained for each outflow boundary condition.

The computational grid, pressure and Mach number distributions in the domain are shown in Fig. 4 for the adiabatic case, which is very similar to the isothermal case not shown here. For the validation of the results, we present a comparison of the surface quantities with the results of [32] for the both cases. In Fig. 5 (top), the surface pressure coefficient of the present solution using different outflow conditions along with the inviscid results of [8,9] are depicted for the both adiabatic and isothermal cases. A close agreement between all outflow conditions can be seen except near the outflow region, where **BC-3** and the results of Kopriva [32] descend to the inviscid pressure and **BC-1**, **BC-1-p** and **BC-4** ascend. The increase/decrease in pressure at the outflow boundary decelerates/accelerates the flow, resulting into the decrease/increase of the nor-

Table 1
Physical conditions for numerical simulation of hypersonic flow over a cylinder.

Case	M_∞	Re_∞	Pr	T_∞(K)	Wall condition	T_w
I	5.73	2050	0.77	39.67	Adiabatic	–
II	5.73	2050	0.77	39.67	Isothermal	5.29

Table 2
Physical conditions for numerical simulation of hypersonic flow over a parabola.

Case	M_∞	Re_∞	Pr	T_∞(K)	Wall condition	T_w
I	15.0	6026.6	0.72	192.989	Isothermal	5.182

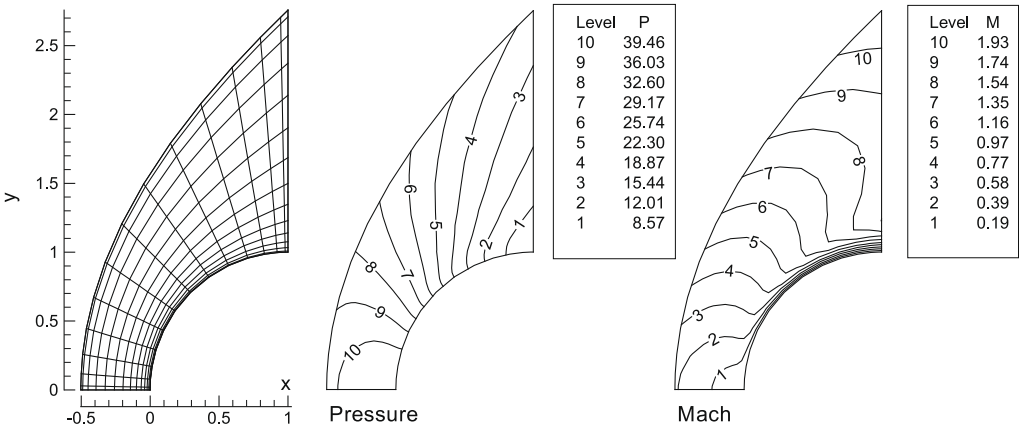

Fig. 4. Computational grid, pressure and Mach number contours for adiabatic cylinder at $M_\infty = 5.73$.

mal gradient of tangential velocity, and therefore, the skin friction coefficient. The skin friction coefficient is plotted for all type of outflow conditions in this figure, which confirms the above explanation. For **BC-3**, the sudden rise of the skin friction coefficient in Fig. 5 (middle), is the obvious penalty of using the inviscid pressure, across the subsonic outflow boundary which shows that the outflow boundary condition used by Kopriva [32–34] is not appropriate one for an accurate computation of the flow field using the spectral scheme. In this figure (bottom), the recovery factor which indicates the extent to which the wall enthalpy recovers to the total enthalpy and the surface heating rate are presented. Along the body surface, when the pressure rises, the flow decelerates. Then, a consequent rise in the internal energy (or the temperature) occurs, and therefore, both the recovery factor and the surface heating rate rise. That is why for the outflow conditions with the pressure rise (**BC-1**, **BC-1-p**, **BC-2**, **BC-4**) indicate higher values of these quantities than usual and vice versa for **BC-3**. Note that for the isothermal case, the results for **BC-3** are nearly consistent with Kopriva [32]. The difference between the results using **BC-3** and Kopriva [32] is that he used a higher outflow pressure value than the inviscid one to match closely with the experimental data [53].

A better perspective on the performance of each outflow condition can be drawn through studying the flow variables across the outflow boundary. The pressure, temperature and Mach number profiles across the outflow boundary are given in Fig. 6 for the both adiabatic and isothermal cases for all outflow conditions together with the inviscid solution [8,9]. All of them have the same behaviour outside the boundary layer; but the distinct effect of each is obvious in the boundary layer especially in the subsonic region. In this figure, there is a large variety of the pressure profiles near the body surface, where **BC-3** and **BC-1**/**BC-1-p** give the lowest and the highest ones, respectively, among the other outflow conditions. As a result, at a distance from the wall, **BC-1** and **BC-1-p** give lower Mach number and higher temperature values among the others and **BC-3** does vice-versa in the subsonic region. For **BC-3**, there is a steep temperature/velocity gradient within the boundary layer than the others, while for **BC-1**/**BC-1-p**, a slight temperature/velocity gradient is observed. In Fig. 6, the temperature at the edge of thermal boundary layer has a noticeable difference for different outflow conditions. In addition, all temperature profiles have a sharp turn near the wall except **BC-3** profile. Within the boundary layer, especially in the subsonic region, it seems that the velocity and temperature normal gradients are considerably influenced by the outflow pressure distribution unlike the thickness of velocity and thermal boundary layers. That is why the shock distance is not changed using all mentioned subsonic outflow conditions. Additionally, there is a strong influence from the subsonic outflow pressure over the supersonic part of the boundary layer. As nearly the same behaviour observed for adiabatic case and isothermal case, the first one is considered only, here after for further study.

The inspection of the effect of each outflow condition on the solution is followed by making use of artificiality aspect of the boundaries through shrinking/extending the body geometry (73°–90°–101°) and finding the corresponding solution (Fig. 3) for the adiabatic case. The flow variables at the points lie on 73°/90° line within the computational domain of 90°/101° body and on the boundary of 73°/90° body should be the same for an outflow condition to be precise. In Figs. 7–10, comparisons are made for the surface quantities of bodies of 73°,90° and 101° arc lengths using each outflow condition for the adiabatic case. In Fig. 7 obvious deviations from the correct surface quantities are seen for **BC-1** and **BC-2**. It is also true for **BC-1-p**, as shown in Fig. 8. For this outflow boundary condition the streamwise Mach number, the weighting parameter, $\bar{\omega}$, and its role on the streamwise pressure gradient and the normal velocity gradient are plotted at the station 90° and they are compared with their correct values. Here, multiplication by $\bar{\omega}$, overcompensates for the streamwise pressure gradient term by adding a positive part to it and follows a non-physical pressure gradient. That is why the pressure coefficient deviates from the correct one. In Fig. 9 (left), the surface pressure coefficient reaches to the inviscid value for **BC-3** at the outflow, making the flow to speed up, the skin friction coefficient to blow up and the recovery factor to fall down near the outflow. In this figure (right), **BC-4** follows the same behaviour as **BC-1** and **BC-1-p** outflow conditions. For **BC-5** and **BC-6**, better results are obtained than the others in Fig. 10. Nearly, all outflow conditions exhibit at least a deviation from

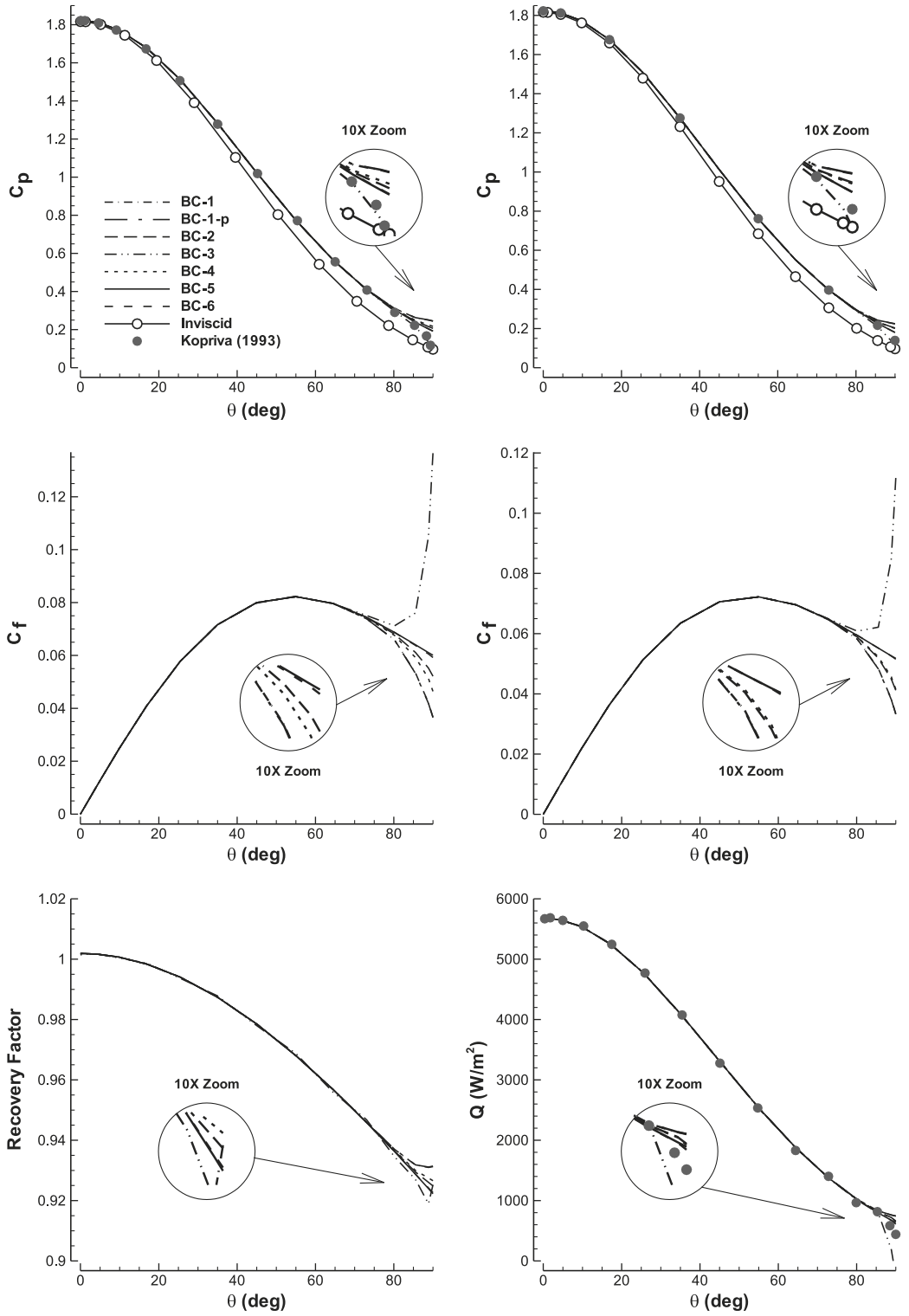

Fig. 5. Surface pressure coefficient, skin friction coefficient, recovery factor and surface heating rate for the adiabatic (left) and isothermal (right) cylinder at $M_\infty = 5.73$ for different outflow conditions.

the exact condition for 73° body, because there are strong interactions of blunt nose effects going on for short computational domains and this emphasizes bearing in mind a limitation for the location of a good artificial computational boundary for

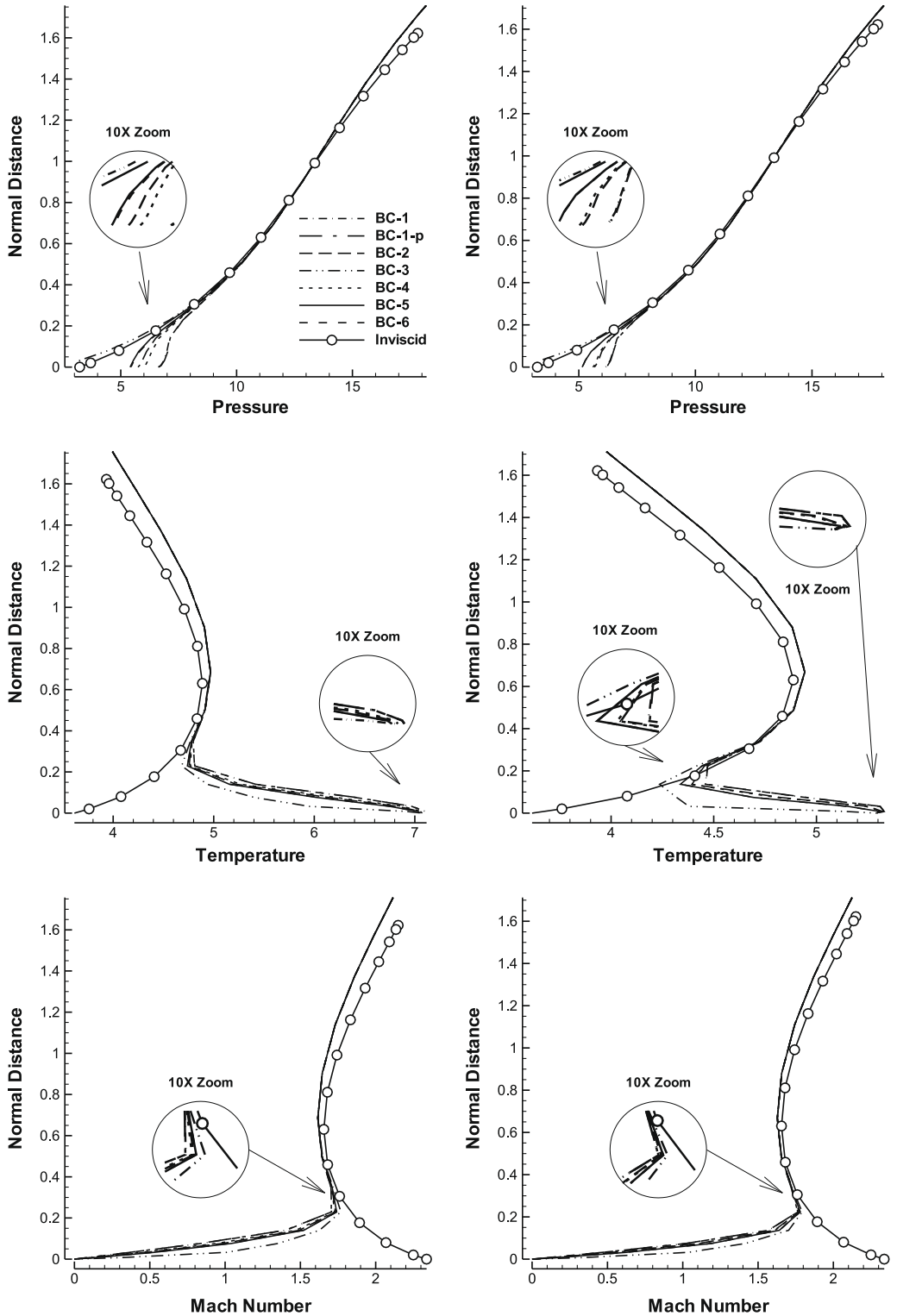

Fig. 6. Profiles of the flow variables across the outflow boundary of the adiabatic (left) and isothermal (right) cylinder at $M_\infty = 5.73$ for different outflow conditions.

this typical problem. From these figures, it can be stated that a little deviation in the pressure in the subsonic outflow region, affects the body surface quantities significantly near that region. Furthermore, the maximum percent of errors are tabulated

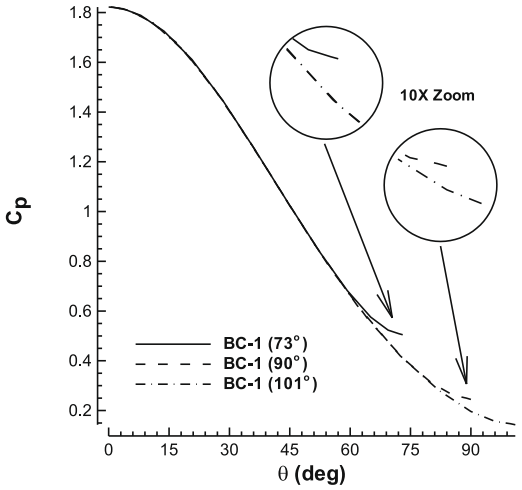

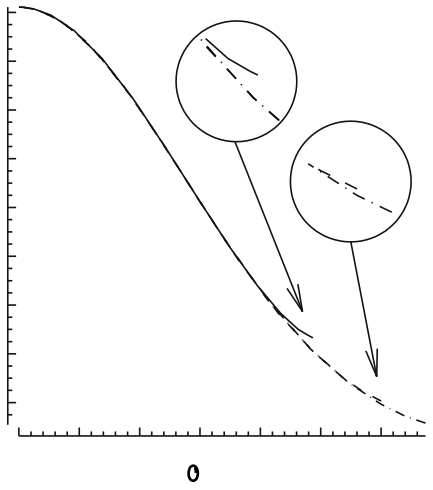

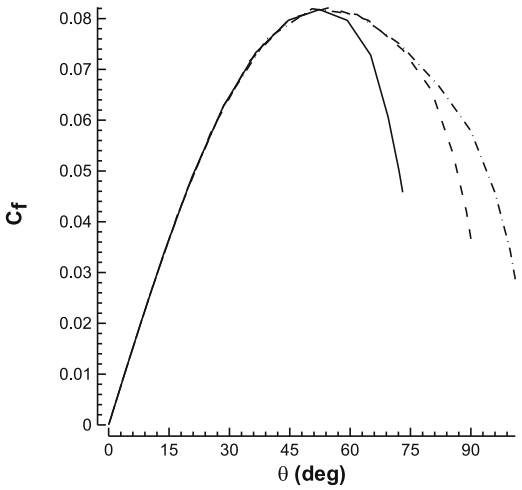

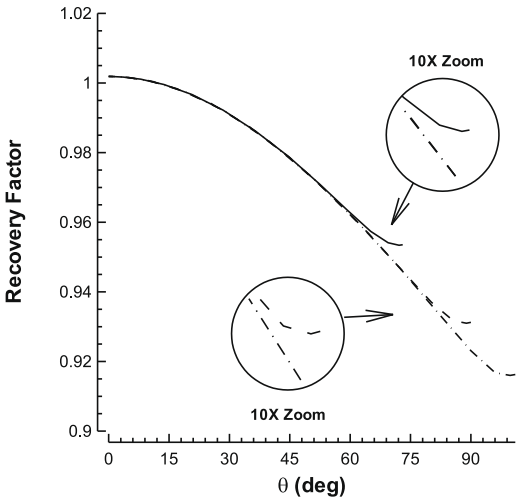

in Table 3 at these stations for the surface pressure coefficient, the skin friction coefficient and the recovery factor. It can be observed that **BC-3** has the highest error value in each quantity and **BC-5** and **BC-6** have the lowest ones, as also seen in

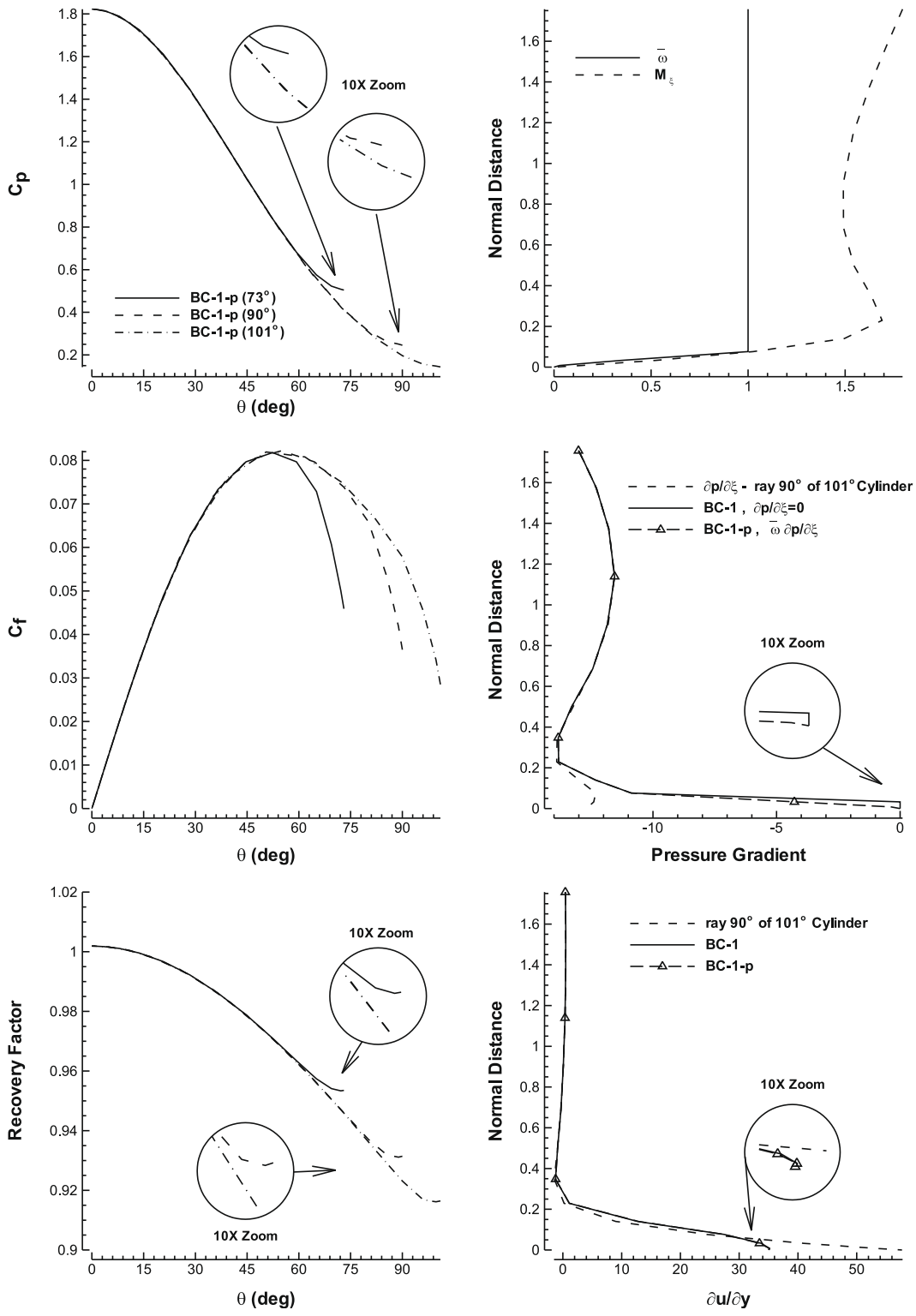

Fig. 8. Surface pressure coefficient, skin friction coefficient and recovery factor for the adiabatic cylinder at $M_\infty = 5.73$ using **BC-1-p** (left column) for different arc lengths and profiles of weighting parameter $\bar{\omega}$, streamwise Mach number, correct and modified streamwise pressure gradient and normal velocity gradient for 90° cylinder (right column).

Fig. 10. Table 3 presents the lowest to the highest overall error values for **BC-5**/**BC-6**/**BC-2**/**BC-4**/**BC-1-p**/**BC-1**/**BC-3**, respectively. For the isothermal case, Table 4 lists the maximum percent of errors at the stations considered for the surface pressure

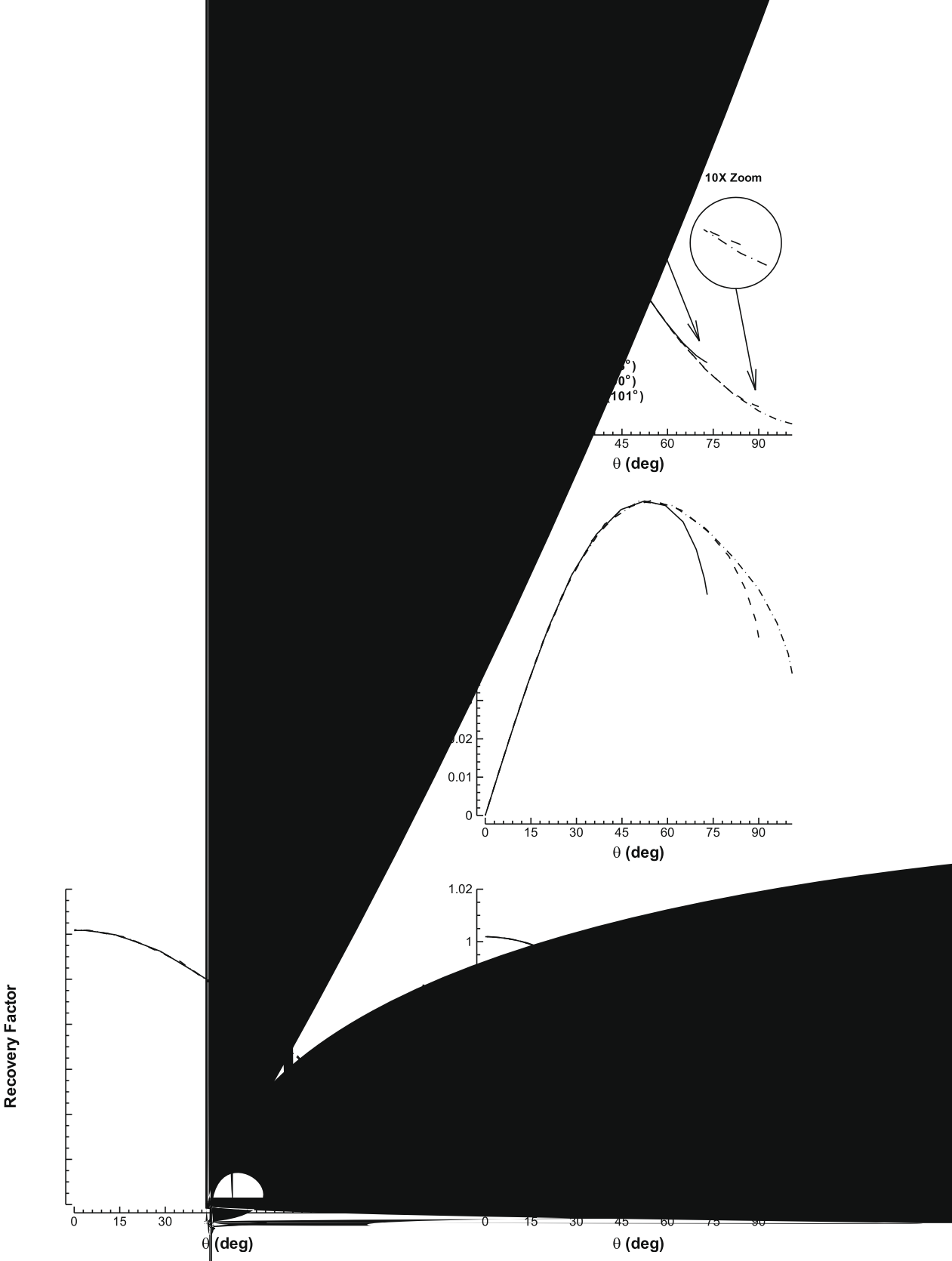

coefficient, the skin friction coefficient and the surface heating rate. In this table, **BC-5**/**BC-6**/**BC-4**/**BC-2**/**BC-1-p**/**BC-1**/**BC-3** have the maximum percent of overall errors in an ascending order. For both the adiabatic and isothermal cases, using **BC-**

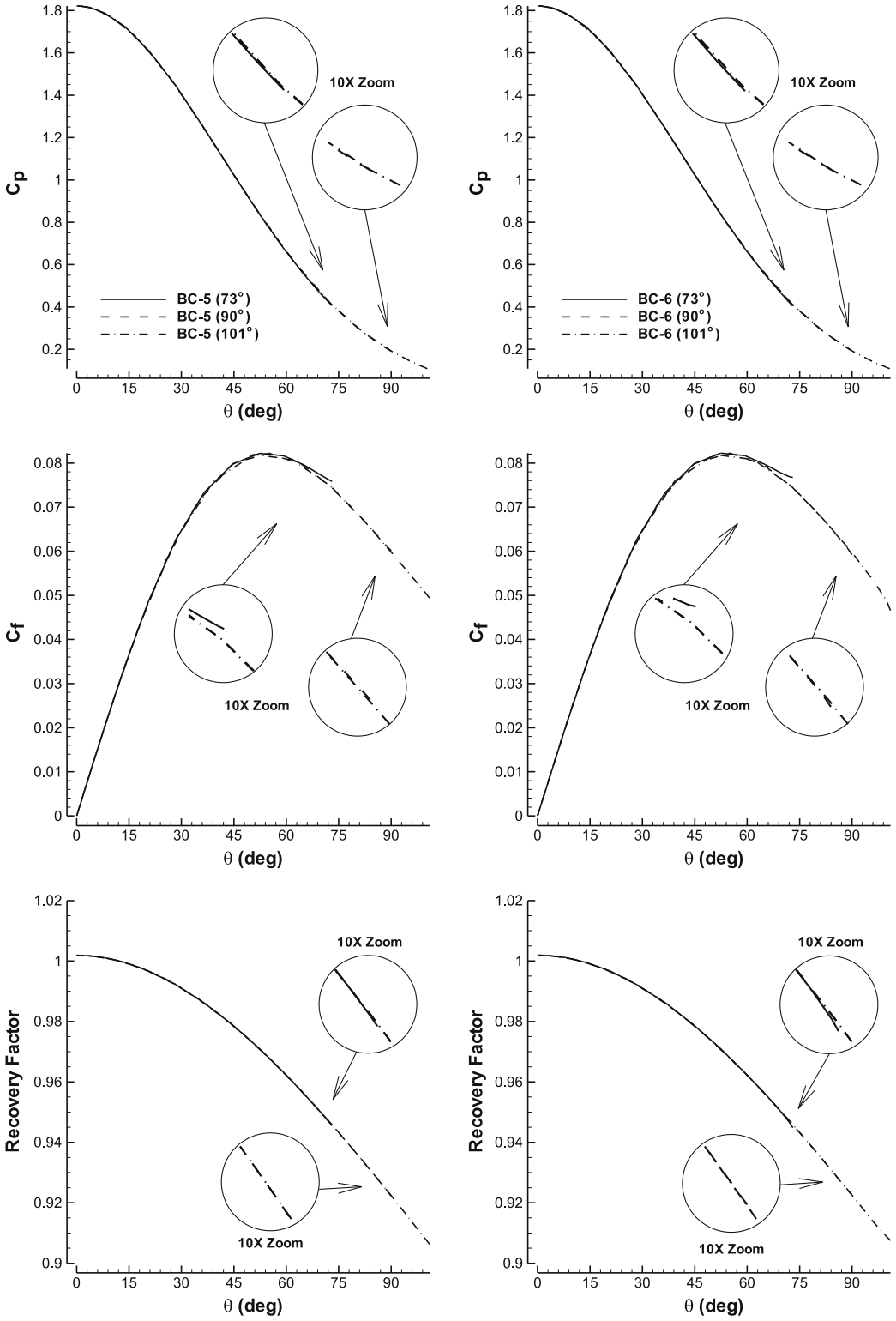

Fig. 10. Surface pressure coefficient, skin friction coefficient and recovery factor for the adiabatic cylinder at $M_\infty = 5.73$ using **BC-5** (left column) and **BC-6** (right column) for different arc lengths.

4, it is observed that there are errors of the same order at both the stations 73° and 90°, which is the consequence of neglecting the reflected characteristic wave amplitude at the subsonic outflow boundary. It is found that **BC-5** and **BC-6** by less than 2% and 3% of error, respectively, are close to the exact subsonic outflow condition for both the stations 73° and 90°.

Table 3
Comparison of the maximum relative error percent in the body surface quantities through body shrink/extension for the adiabatic cylinder at $M_\infty = 5.73$ using different outflow conditions.

	Station angle	Maximum error percent in pressure coefficient	Maximum error percent in skin friction coefficient	Maximum error percent in recovery factor
BC-1	73°	22.70	37.99	0.80
	90°	24.53	36.70	0.88
BC-1-p	73°	22.59	37.84	0.80
	90°	25	36.86	0.90
BC-2	73°	13.54	24.6	0.47
	90°	6.91	12.15	0.24
BC-3	73°	25.42	64.41	0.87
	90°	48.44	119.31	0.17
BC-4	73°	11.24	22.40	0.41
	90°	11.95	21.33	0.42
BC-5	73°	0.86	1.89	0.04
	90°	0.35	0.40	0.01
BC-6	73°	1.43	3.47	0.05
	90°	0.13	0.69	0.11

Table 4
Comparison of the maximum relative error percent in the body surface quantities through body shrink/extension for the isothermal cylinder at $M_\infty = 5.73$ using different outflow conditions.

	Station angle	Maximum error percent in pressure coefficient	Maximum error percent in skin friction coefficient	Maximum error percent in heating rate
BC-1	73°	18.47	33.66	5.04
	90°	22.18	33.96	15.42
BC-1-p	73°	18.35	33.5	5.05
	90°	22.59	34.18	15.76
BC-2	73°	11.09	21.65	1.22
	90°	11.67	19.53	3.42
BC-3	73°	22.96	59.29	7.41
	90°	45.77	127.99	99.86
BC-4	73°	8.96	19.23	0.5
	90°	9.95	18.57	1.87
BC-5	73°	0.71	1.61	0.64
	90°	0.61	0.76	0.56
BC-6	73°	1.17	2.96	1.88
	90°	0.76	0.55	2.4

The profiles of different flow variables at the outflow boundary like pressure, temperature and Mach number are plotted in Figs. 11–17 as a function of the normal distance for each outflow condition. There are good agreements for all outflow conditions for the most part out of the boundary layer. Fig. 11 shows that **BC-1**, that removes the streamwise pressure gradient term completely, over-predicts the pressure and temperature values and under-predicts the Mach number in both the stations 73° and 90°. In Fig. 12, the same trend can be observed for **BC-1-p** that removes the elliptic part of the streamwise pressure gradient. Although a stable solution is obtained, the computed pressure has a noticeable deviation from the exact one for both **BC-1** and **BC-1-p**. The adiabatic wall temperature and the temperature at the boundary layer edge are over-predicted by these outflow conditions. Also, the normal gradient of velocity is under-predicted, that is why the skin friction coefficient is fallen down in Figs. 7 and 8 (left).

The outflow condition based on the sublayer approximation, **BC-2**, slightly over-predicts the pressure at the outflow of 73° body, as depicted in Fig. 13. This approximation becomes more accurate for 90° body. In Fig. 14, **BC-3** under-predicts the pressure at the outflow of 73° and 90°. A noticeable difference between the inviscid pressure profile and the exact one can be seen in Fig. 14 for **BC-3**. The variation of the exact pressure across the boundary layer is another observation seen in this figure. Thus, **BC-3** falls undoubtedly into errors of inviscid as well as constancy of the pressure approximation. The more steep velocity and temperature gradients than the exact ones are other outcomes. Additionally, the sharp variation of the normal derivative of pressure may cause unexpected oscillating artifacts within the solution due to the global char-

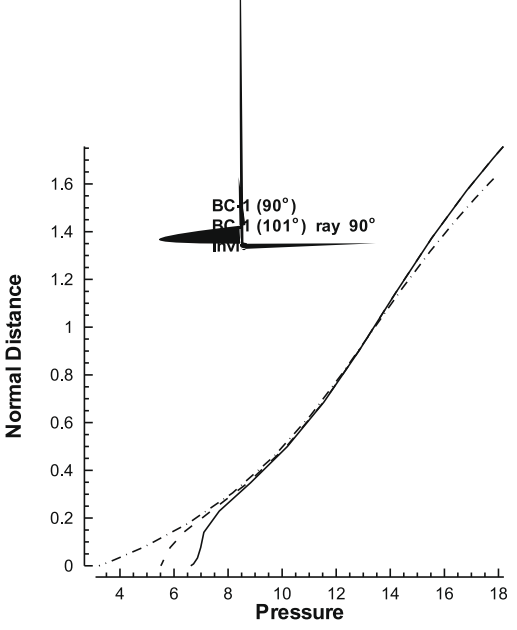

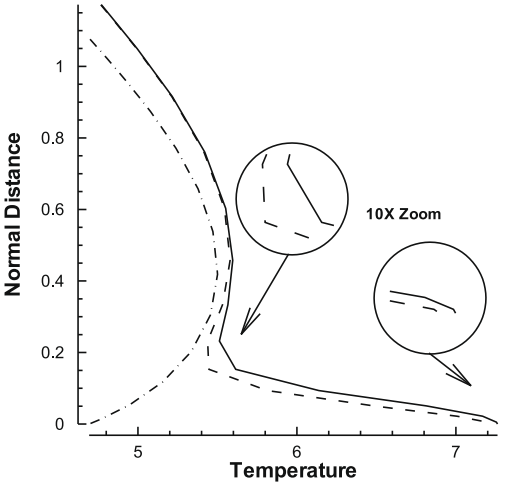

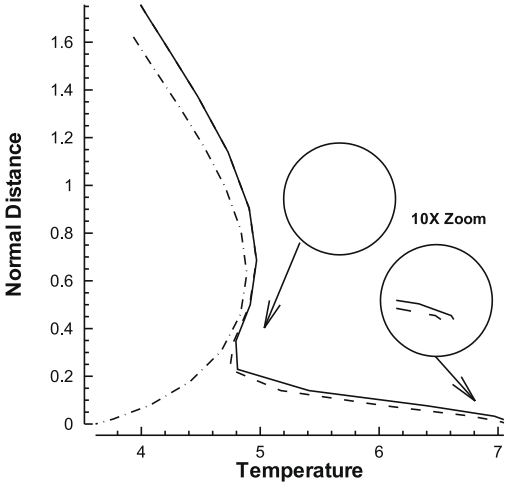

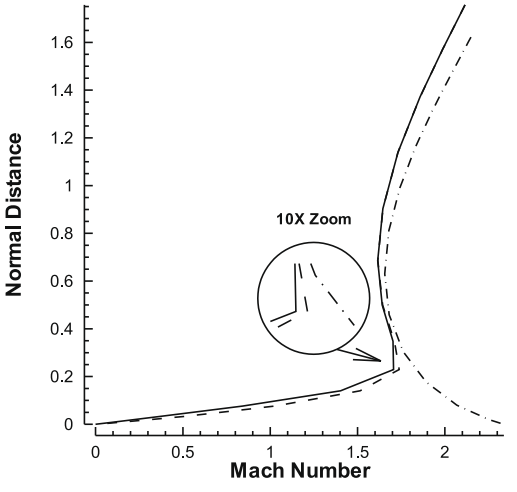

acter of the spectral approximations. In Fig. 15, **BC-4** over-predicts the pressure and under-predicts the velocity and the temperature gradients within the boundary layer. **BC-5** and **BC-6** agree nearly precise with the exact profiles, as depicted in Figs.

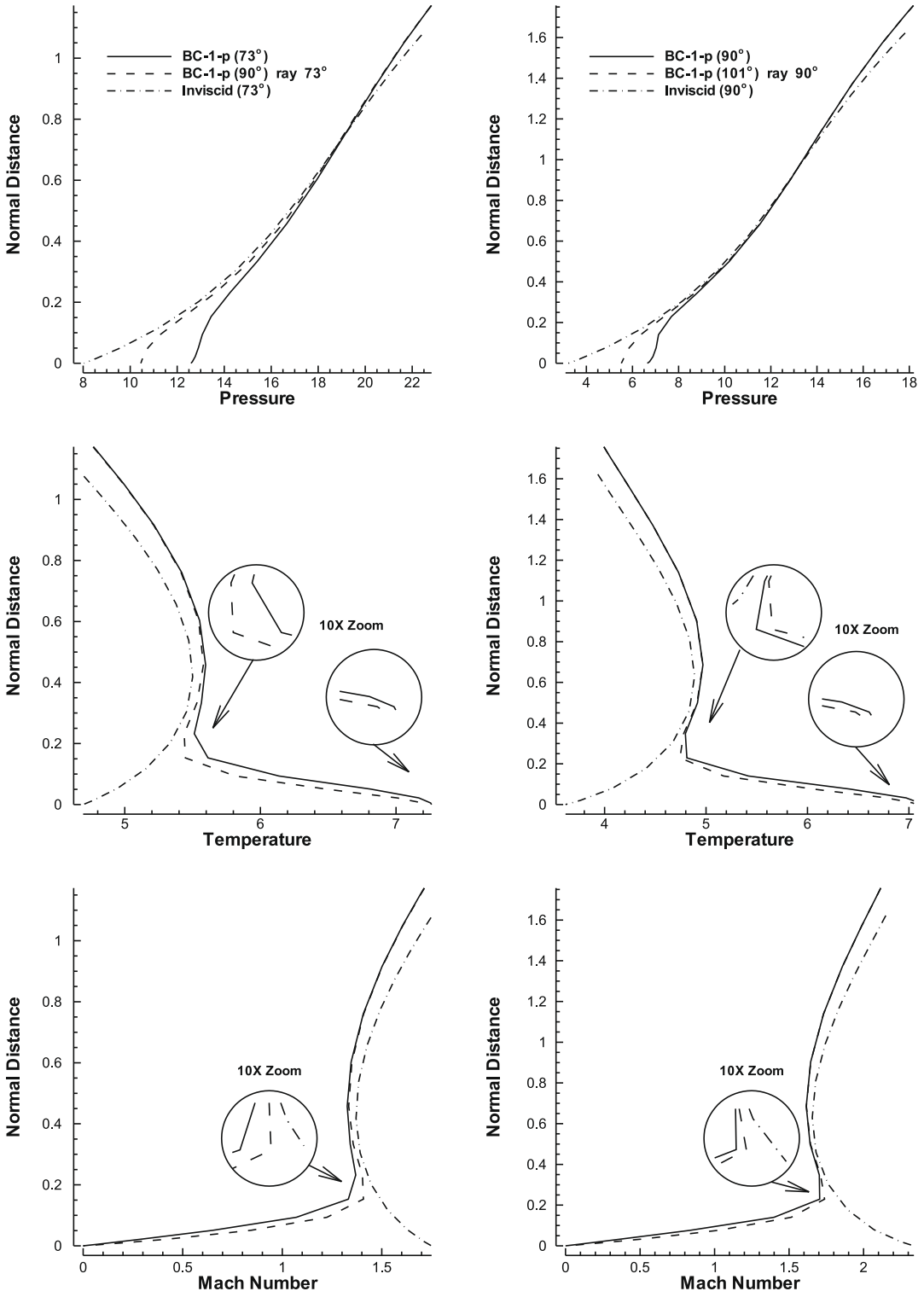

Fig. 12. Profiles of the flow variables across the outflow boundary of the adiabatic cylinder at $M_\infty = 5.73$ using **BC-1-p** for two different arc lengths (73° left column and 90° right column).

16 and 17, respectively. Therefore, these two outflow boundary conditions can provide more accurate solutions than the others. It is clear that for all outflow boundary conditions used, the deviation from the exact condition diminishes as the gradients of flow variables decrease along the body.

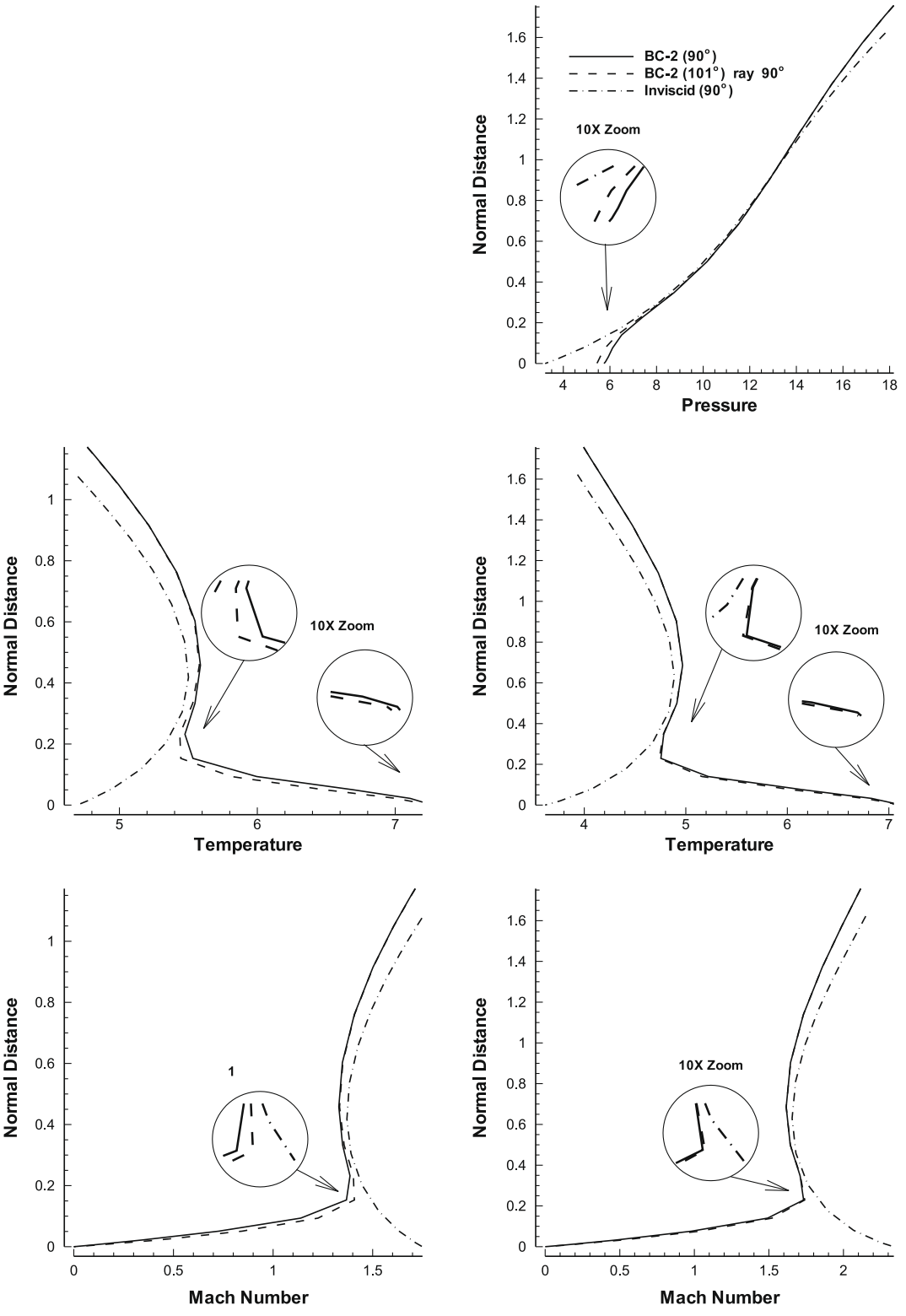

Listed in Tables 5 and 6 are the percent of maximum relative error in the pressure, temperature, velocity, vorticity and entropy variables across the outflow boundary through body shrink/extension for the adiabatic and isothermal cases,

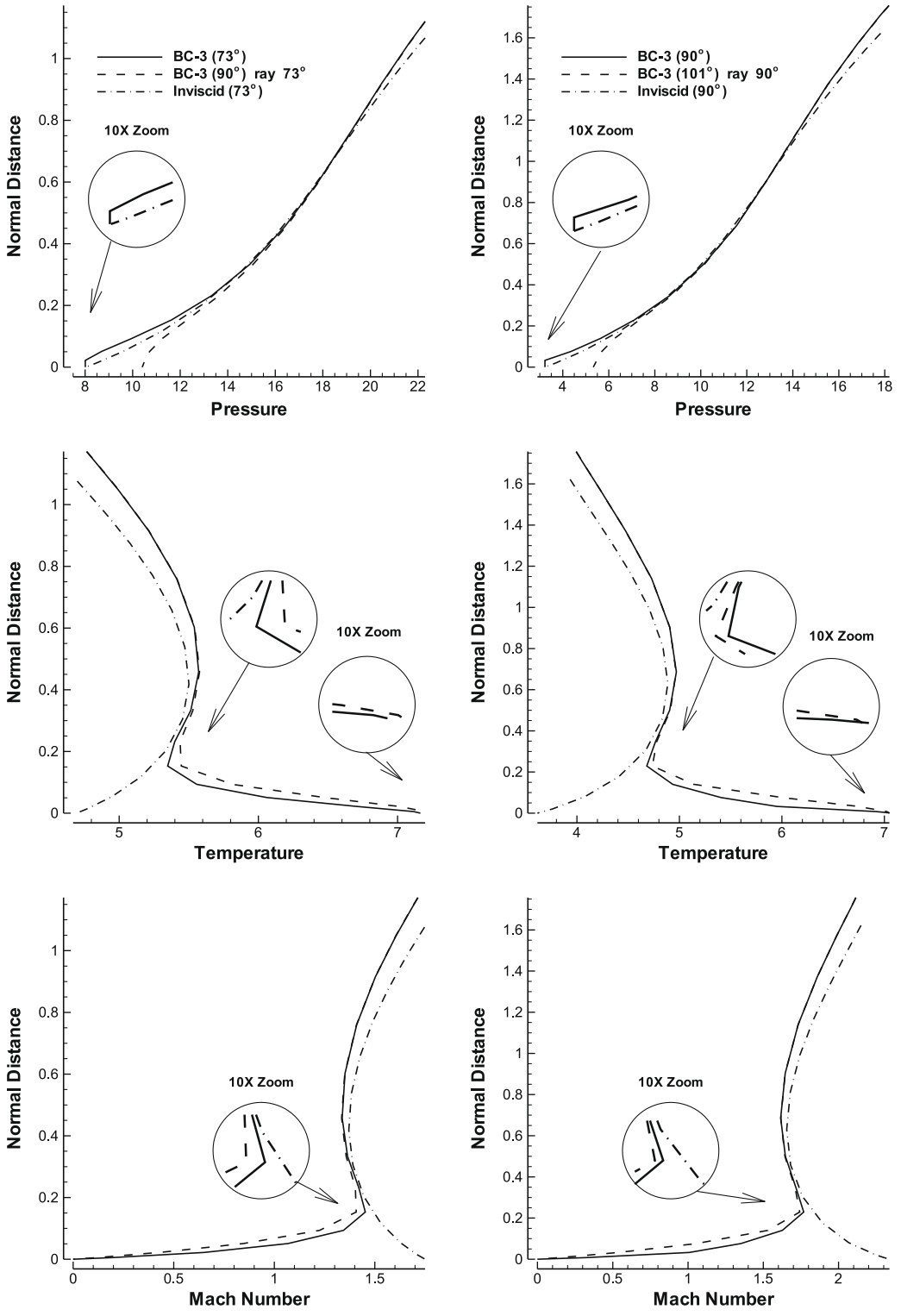

Fig. 14. Profiles of the flow variables across the outflow boundary of the adiabatic cylinder at $M_\infty = 5.73$ using **BC-3** for two different arc lengths (73° left column and 90° right column).

respectively. It is observed that **BC-5**/**BC-6**/**BC-2**/**BC-4**/**BC-1-p**/**BC-1**/**BC-3** have the least average error in an ascending order. Note that **BC-1-p** gives slightly better results than **BC-1**, as it considers the hyperbolic part of the streamwise pressure gradient.

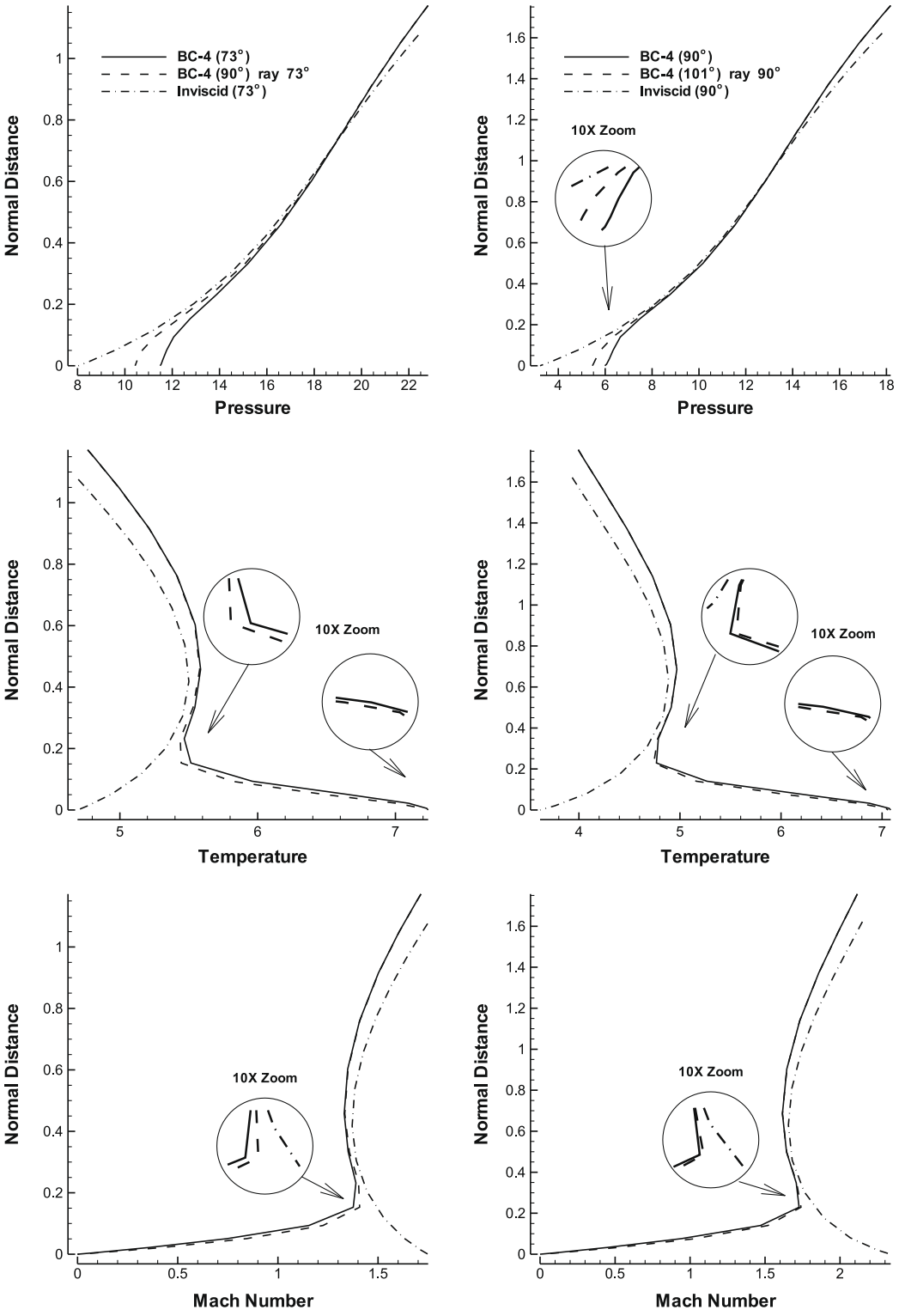

Fig. 15. Profiles of the flow variables across the outflow boundary of the adiabatic cylinder at $M_\infty = 5.73$ using **BC-4** for two different arc lengths (73° left column and 90° right column).

Up to here, it is demonstrated that **BC-5** and **BC-6** promise accurate results compared with other outflow boundary conditions. Comparisons with other researchers' results and experiments for the body surface quantities are made in

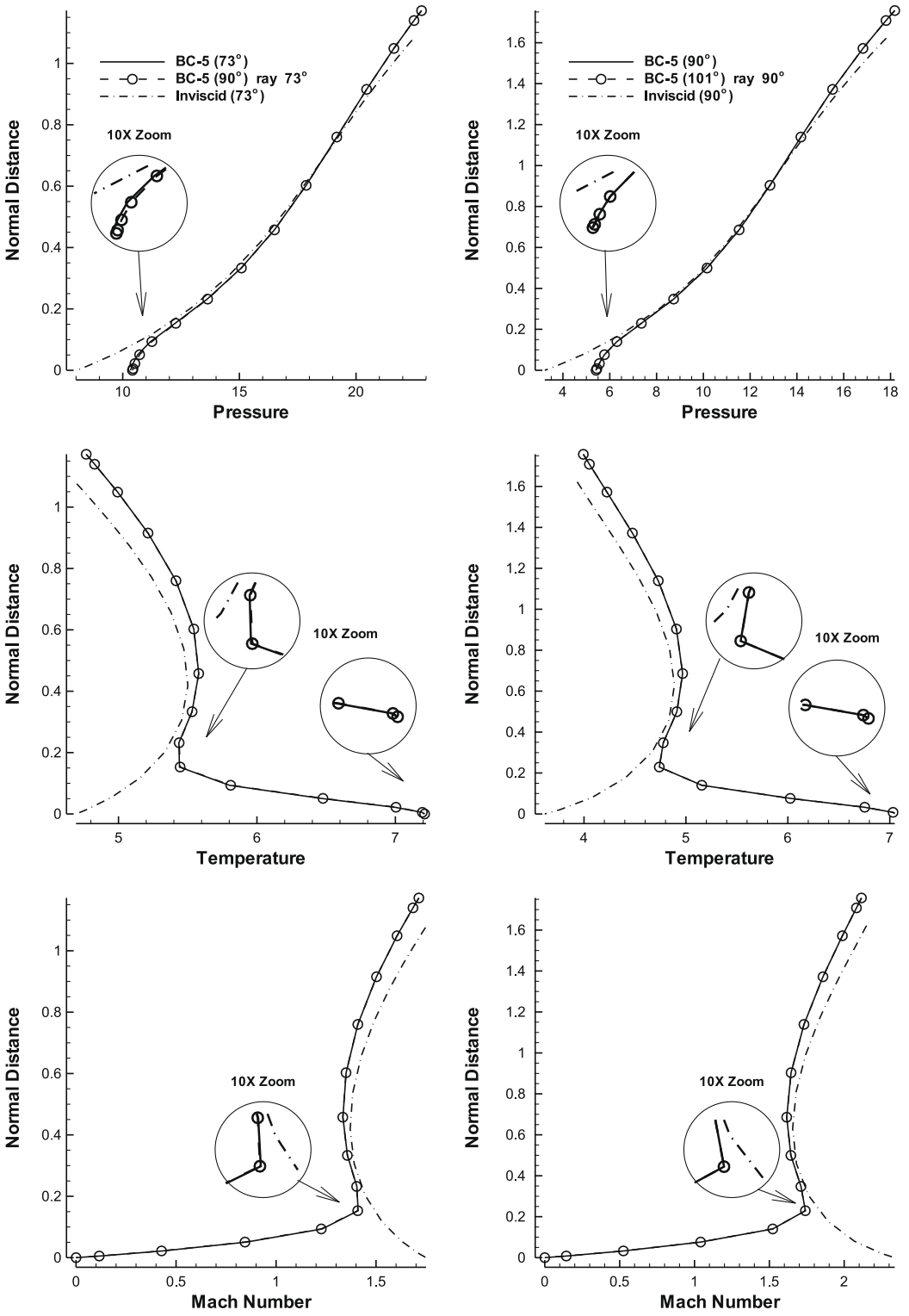

Fig. 16. Profiles of the flow variables across the outflow boundary of the adiabatic cylinder at $M_\infty = 5.73$ using **BC-5** for two different arc lengths (73° left column and 90° right column).

Fig. 18 for the adiabatic and isothermal cases. The surface pressure coefficient distribution computed by the present solution employing **BC-5** and **BC-6** using (15×15) grid points agrees well with the thin-layer Navier–Stokes (TLNS)

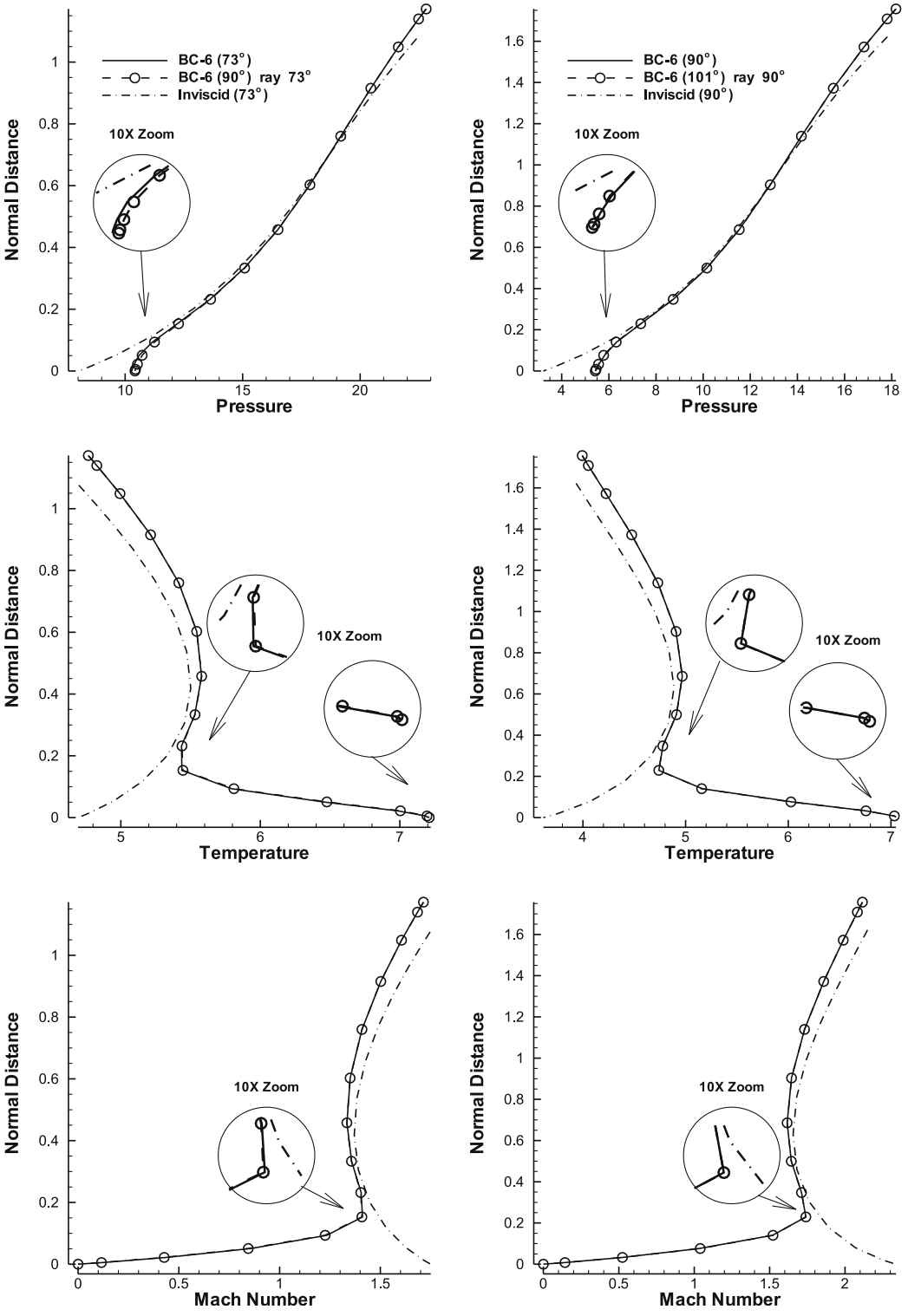

Fig. 17. Profiles of the flow variables across the outflow boundary of the adiabatic cylinder at $M_\infty = 5.73$ using **BC-6** for two different arc lengths (73° left column and 90° right column).

results by Esfahanian [51] using the Beam-Warming method with (40×100) and (40×150) grid points, the second-order finite-difference method by Gnoffo [52] with (51×50) grid points, the fifth-order upwind compact finite-difference

Table 5
Comparison of the maximum relative error percent in flow variables at the outflow boundary through body shrink/extension for the adiabatic cylinder at $M_\infty = 5.73$ using different outflow conditions.

	Station angle	Maximum error percent in pressure	Maximum error percent in temperature	Maximum error percent in velocity	Maximum error percent in vorticity	Maximum error percent in entropy
BC-1	73°	21.05	5.57	36.76	38.32	6.3
	90°	21.48	5.85	34.69	37.07	6.16
BC-1-p	73°	20.94	5.55	36.58	38.17	6.27
	90°	21.8	6.00	34.76	37.24	6.25
BC-2	73°	12.47	3.2	23.65	24.84	3.97
	90°	6.34	1.86	11.43	12.3	1.91
BC-3	73°	23.82	6.41	64.89	65.38	9.84
	90°	41.14	11.69	117.28	118.7	22.89
BC-4	73°	10.3	2.64	20.73	22.61	3.32
	90°	10.34	2.97	19.1	21.55	3.19
BC-5	73°	0.82	0.22	1.79	2.1	0.28
	90°	0.29	0.04	0.47	0.59	0.1
BC-6	73°	2.34	0.65	4.97	5.21	0.72
	90°	0.75	0.27	0.74	5.02	0.1

Table 6
Comparison of the maximum relative error percent in flow variables at the outflow boundary through body shrink/extension for the isothermal cylinder at $M_\infty = 5.73$ using different outflow conditions.

	Station angle	Maximum error percent in pressure	Maximum error percent in temperature	Maximum error percent in velocity	Maximum error percent in vorticity	Maximum error percent in entropy
BC-1	73°	16.96	4.19	31.68	33.66	5.97
	90°	18.62	5.07	31.16	33.96	6.38
BC-1-p	73°	16.84	4.16	31.49	33.49	5.94
	90°	18.99	5.18	31.47	34.18	6.49
BC-2	73°	10.1	2.56	20.21	21.65	3.74
	90°	9.99	2.65	17.97	19.53	3.54
BC-3	73°	21.54	5.23	57.18	59.29	9.72
	90°	37.4	15	98.99	111.78	20.26
BC-4	73°	8.13	2.01	17.11	19.23	3.06
	90°	8.43	2.2	16.27	18.57	3.04
BC-5	73°	0.67	0.18	1.47	1.61	0.26
	90°	0.49	0.07	0.74	0.76	0.2
BC-6	73°	1.14	0.29	2.65	2.96	0.42
	90°	0.62	0.04	0.81	1.55	0.25

method by Zhong [30] with (60×80) grid points and also the experimental results by Tewfik and Giedt [53] for both the adiabatic and isothermal cases. For the skin friction coefficient, a good agreement is observed with [51] which shows the accuracy of the outflow boundary conditions implemented. In these figures, near the outflow, the difference in the recovery factor/surface heating rate between the present results and those of TLNS [51] may be due to the different type of governing equations used.

The convergence history of the density residual and the shock velocity for all outflow conditions together with the inviscid solution (with the same CFL) are demonstrated in Fig. 19 for both the adiabatic and isothermal cases. The inviscid solution has the lowest convergence rate, probably because of low dissipation of the spectral method and the reflection of spurious waves from boundaries due to inappropriate initial condition used. The viscous solutions converge rapidly for all outflow conditions nearly at the same rate, due to existence of physical dissipation. For the isothermal case, **BC-3** converges slower than the others, probably due to the use of the constant pressure distribution at the subsonic outflow.

For different outflow conditions, the grid convergence error studies are provided for 73° and 90° cylinders. For the viscous blunt-body problem, it is difficult to perform an accuracy analysis when using a shock-fitting technique. In fact, the flow field is under the influence of the shock position and the boundary layer. On the other hand, the grid stretching used near the wall for better resolution of velocity and thermal boundary layers, may decrease the grid convergence rate of spectral collocations

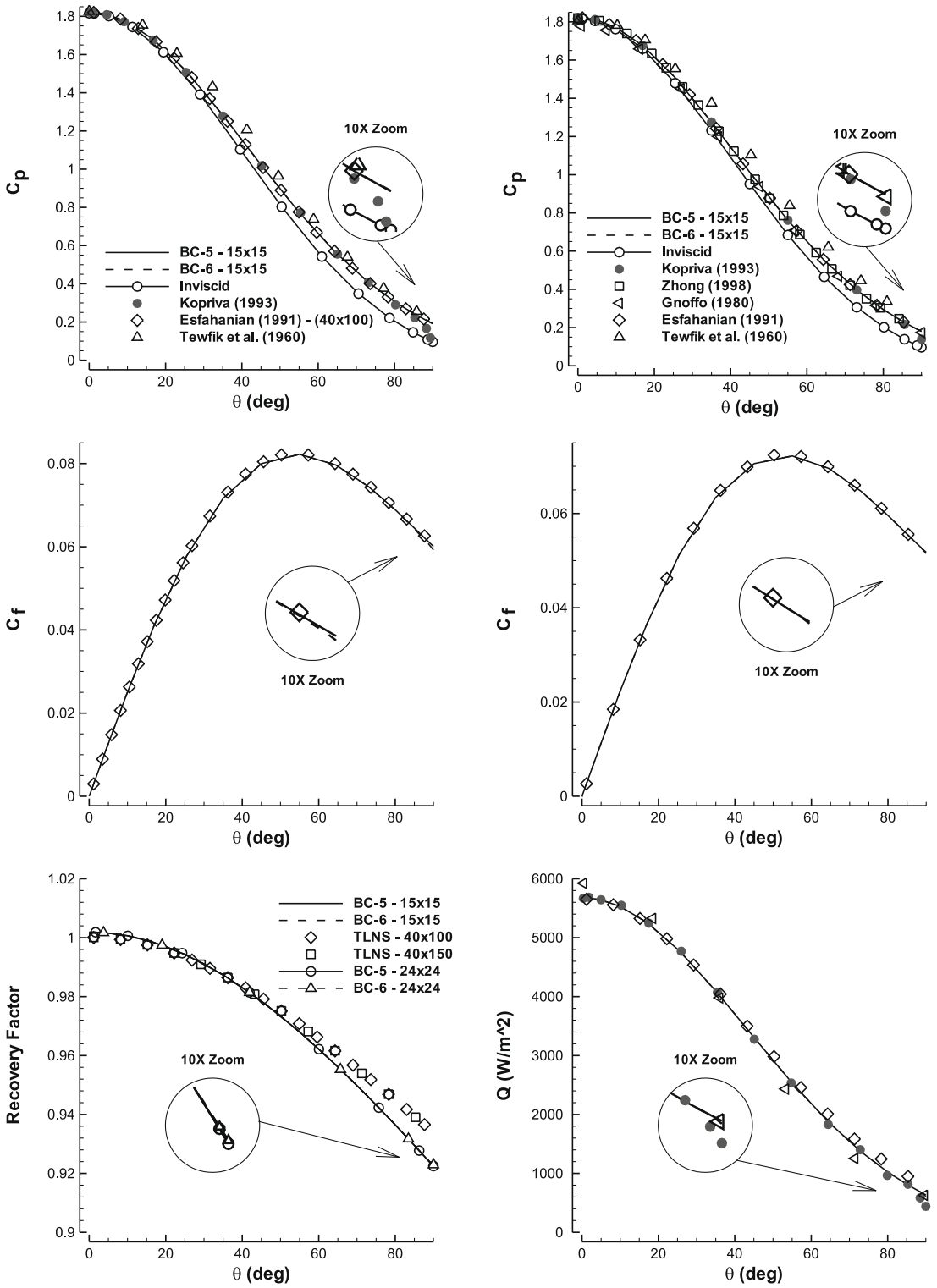

Fig. 18. Surface pressure coefficient, skin friction coefficient, recovery factor and surface heating rate for the adiabatic (left column) and isothermal (right column) cylinder at $M_\infty = 5.73$ for **BC-5** and **BC-6** compared with other researchers' results and experimental data.

and for some cases, may produce oscillations [49]. For such reasons, we present a grid convergence study for 73° and 90° cylinders without any stretching near the wall boundary for this problem using **BC-5** and **BC-6** outflow conditions. For

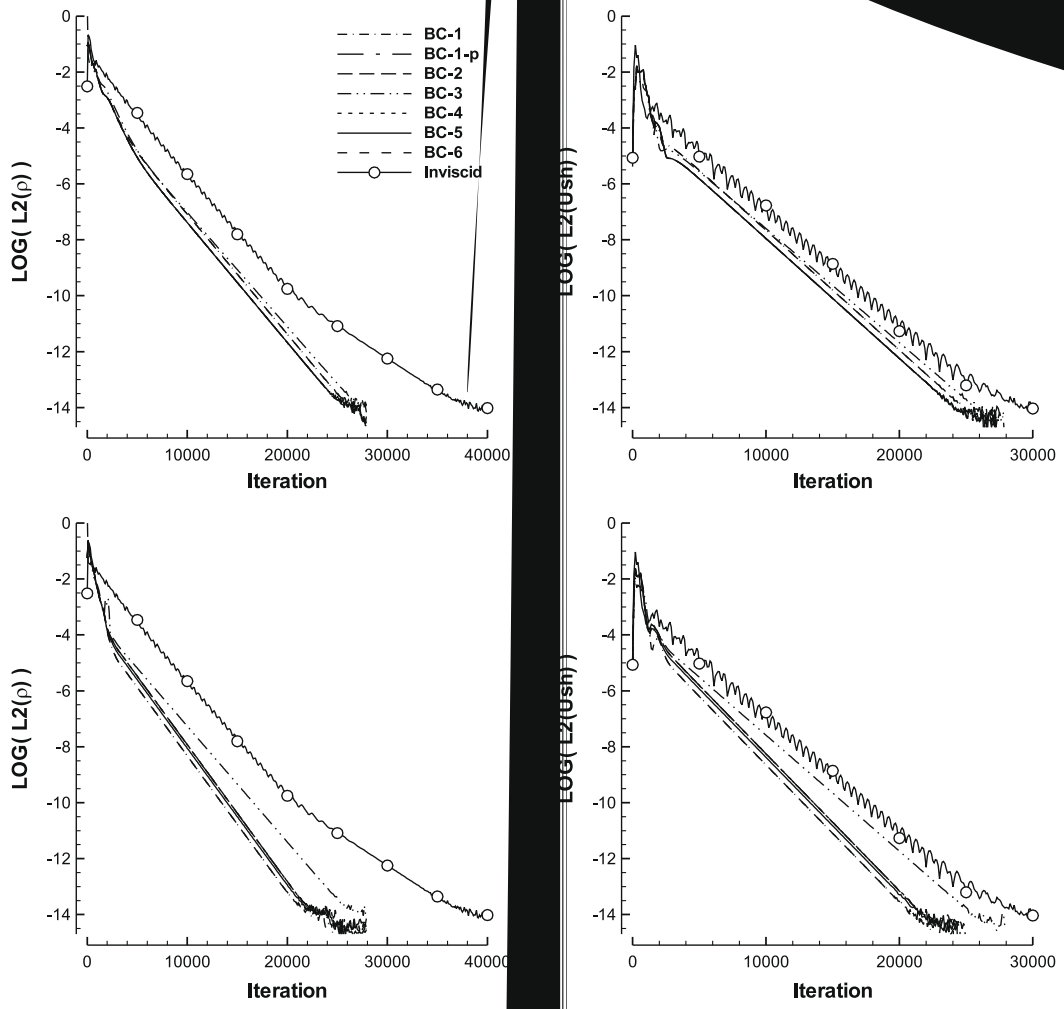

Fig. 19. Convergence history of density residual and shock velocity for th[illegible]batic (first row) and isothermal (second row) cylinder at $M_\infty = 5.73$ using different outflow conditions.

Table 7
Freestream conditions for further assessment of **BC-5** and **BC-6** outflow conditions.

M_∞	2.5			5.73			15		
Re_∞	400	2050	10,000	400	2050	10,000	400	2050	10,000

the 73° case, a (18×24) grid is set as the reference grid and the subsequent grid sets are: $(18 \times 8), (18 \times 10), (18 \times 12), (18 \times 14), (18 \times 16), (18 \times 18), (18 \times 20)$ and (18×22). For the 90° case, a (24×24) grid is set as the reference grid and subsequent grid sets are $(24 \times 8), (24 \times 10), (24 \times 12), (24 \times 14), (24 \times 16), (24 \times 18), (24 \times 20)$ and (24×22). In Fig. 20, the decay of error in L_2 norms for the pressure and temperature in the flow field for the proposed outflow conditions are shown. The small domain (73°) with fewer grid points has nearly the same convergence rate as in the large domain (90°) with more grid points. For a fixed grid size, the error in the smaller domain is less than the larger one. These confirm that for the spectral accuracy, one should increase both the domain size and the number of grid points [4].

In order to study the applicability and performance of the proposed outflow conditions to predict the flow field at different range of Mach and Reynolds numbers, for the 73°, 90° and 101° adiabatic cylinders, a set of test cases is considered as in Table 7. In these cases, the Mach number varies from 2.5 to 15 and the Reynolds number varies from 400 to 10,000. For each outflow condition, the flow variables at the outflow boundary of 73° and 90° cylinders are compared with their internal counterparts. The results for the pressure, temperature and Mach number profiles along the outflow are depicted in Figs. 21 through 24 for the both **BC-5** and **BC-6** outflow conditions. A noticeable boundary layer thickness for low Reynolds number (in Figs. 21 and 22) or low Mach number (in Figs. 23 and 24) flows is seen. This has made the shock to stand farther than other cases, and the shock layer becomes thicker. In low Reynolds numbers and high Mach numbers, the viscous effects are strong and a smooth part is seen near the wall boundary layer edge. In these cases, the thickness of the subsonic part of the outflow is considerable. When this part becomes the dominate part of the boundary layer, **BC-5** and **BC-6** are expected to deviate from the exact outflow condition. With increasing Mach number and decreasing Reynolds number, the thickness of the boundary layer increases and the results based on **BC-5** and **BC-6** are expected to deviate from the exact ones. The study shows that for moderate Mach and Reynolds numbers, both **BC-5** and **BC-6** can provide accurate solutions. Note that for all cases, **BC-5** has better performance than **BC-6**. This might be of the considerable viscous effects in low Reynolds numbers, that are not appropriately considered in the compatibility relations used in **BC-6**. In all cases studied herein, as the region between the boundary layer and the shock is supersonic at the outflow, the proposed outflow conditions, **BC-5** and **BC-6** exhibit good performance.

6.2. Parabola at Mach 15

Another test case is considered to further study the outflow boundary conditions, in simulating viscous hypersonic flow over a different geometry with small surface curvature variations. Here, a parabolic leading edge (parabola) with nose radius of curvature of $R_{nose} = 12.5$ mm is placed in a hypersonic flow, as described in Table 2. A (18×16) grid size with the stretching factor of $\sigma = 0.8$ in the wall-normal direction is used for the numerical simulation (see Fig. 25). The time integration is progressed using CFL = 2.5 until the steady state solution is reached. A convergent solution is attained for each outflow boundary condition.

The computational grid, pressure and Mach number contours over the geometry are presented in Fig. 25 for this test case. For different outflow boundary conditions, the surface pressure coefficient, the skin friction coefficient, the surface heating rate normalized to its stagnation value and the profiles of flow variables across the outflow are depicted in Fig. 26. Close agreements are observed among all outflow conditions except for the region near the outflow. As the pressure estimation concerns, the same reasons for deviations can be made as stated for Fig. 5 in previous test case. Unlike the cylinder case, small surface curvature variations made all outflow conditions to operate somehow well except for **BC-3**. The pressure for **BC-3** approaches to the inviscid pressure within the boundary layer. The constancy of subsonic outflow pressure for this outflow boundary condition is quite clear in this figure. It can be seen again that the pressure in the supersonic part of the boundary layer is affected firmly by the subsonic part, which is beyond doubt for **BC-3**. Only little differences exist among the other outflow conditions and they are almost identical. The temperature and Mach number profiles and also the normalized surface heating rate distributions are very similar for all subsonic outflow conditions considered.

In the test cases considered in this study, it is revealed that **BC-5** and **BC-6** exhibit better accuracy and efficiency at the outflow among the others. Here, these two subsonic outflow boundary conditions are selected to make further verification evidence. Compared in Fig. 27 are the pressure and vorticity distributions just behind the bow shock and on the body surface obtained using **BC-5** and **BC-6** with the fifth-order compact finite-difference results of (160×120) grid size by Zhong [30], which agree well together. The distinct difference between the vorticity behind the curved shock and on the body surface indicates the noticeable contribution of the wall in the vorticity generation in this test case. This figure shows the efficiency and high accuracy of the present scheme that uses 1/60 of grid size, and therefore, less computational resources are employed.

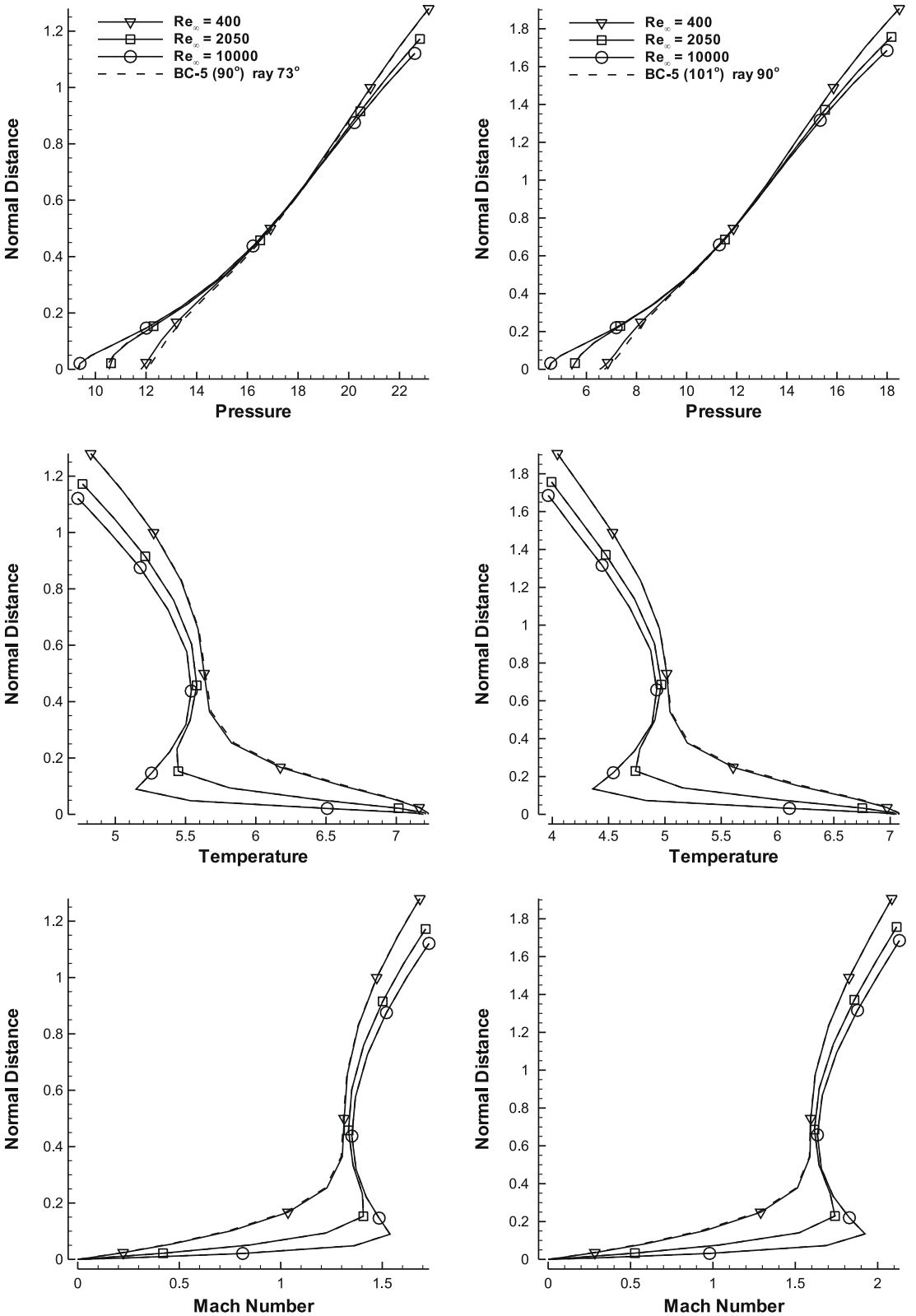

Fig. 21. Profiles of the flow variables across the outflow boundary of the adiabatic cylinder at $M_\infty = 5.73$ using **BC-5** for different Reynolds numbers and for two different arc lengths (73° left and 90° right). The dashed lines represent the values at internal counterpart from a large domain (90° for the left column and 101° for the right column).

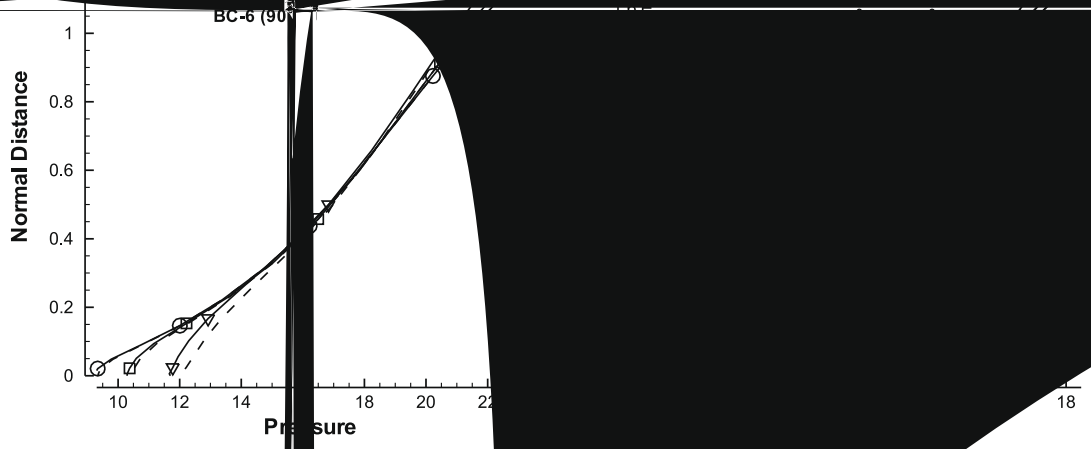
Normal Distance
Pressure

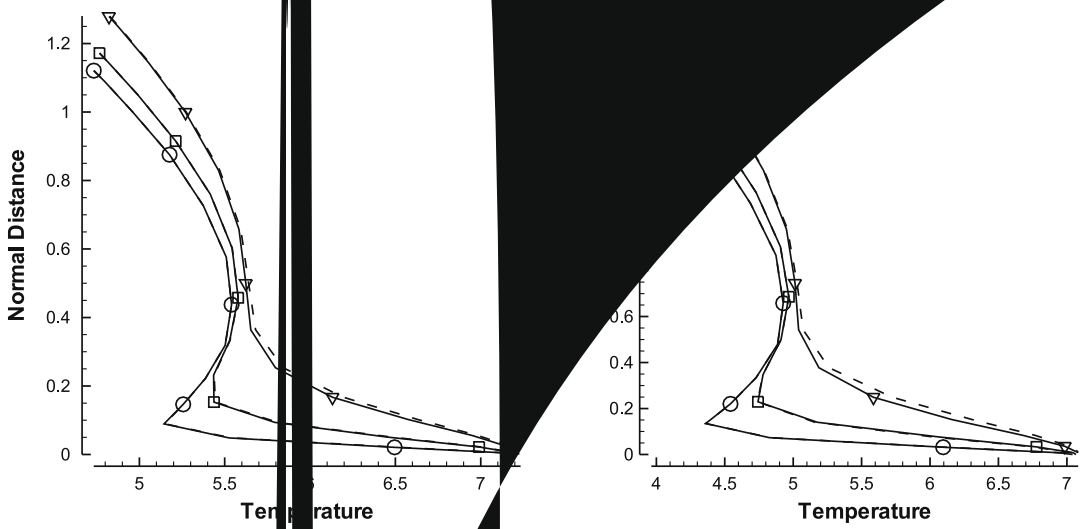
Normal Distance
Temperature

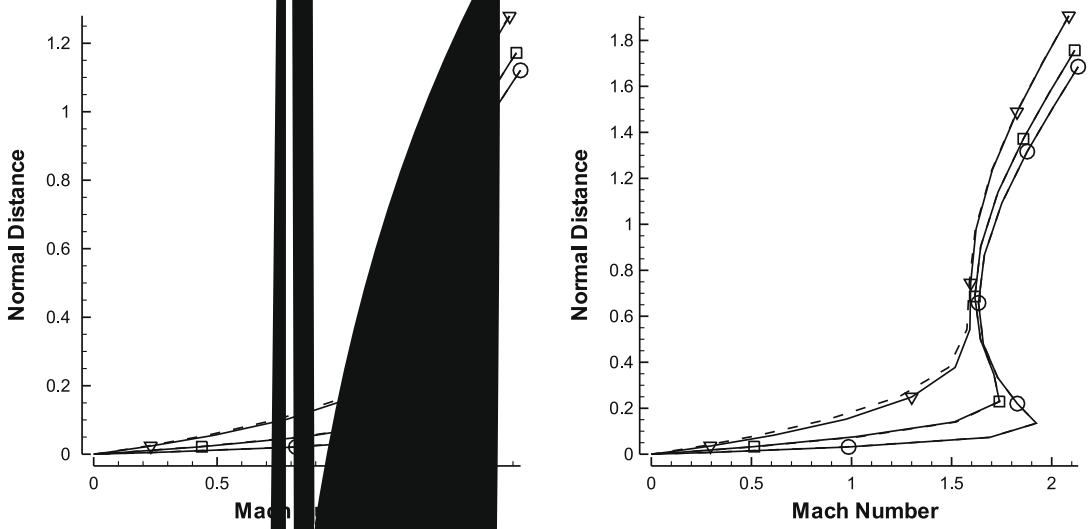
Normal Distance
Mach Number

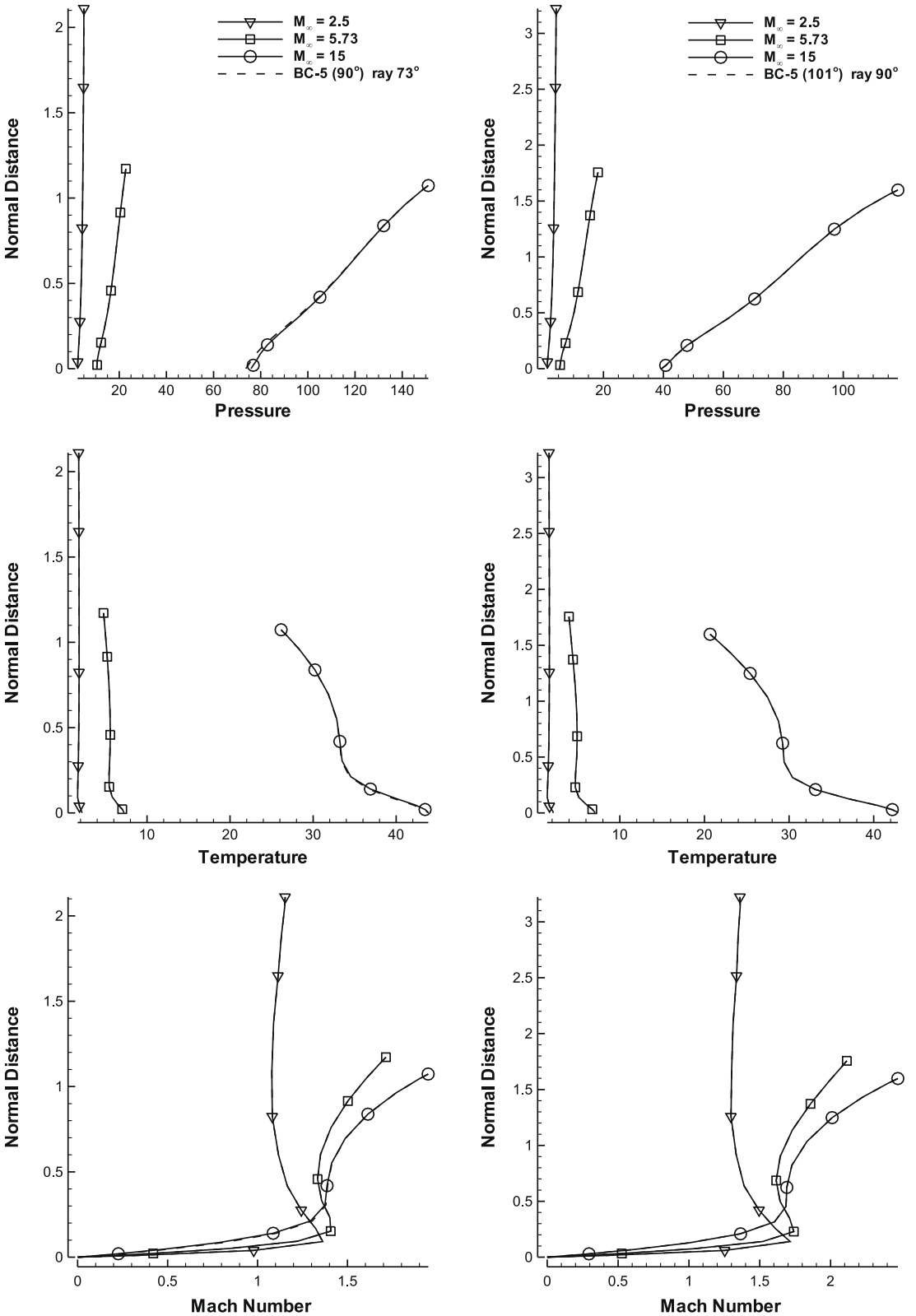

Fig. 23. Profiles of the flow variables across the outflow boundary of the adiabatic cylinder at $Re_\infty = 2050$ using **BC-5** for different Mach numbers and for two different arc lengths (73° left and 90° right). The dashed lines represent the values at internal counterpart from a large domain (90° for the left column and 101° for the right column).

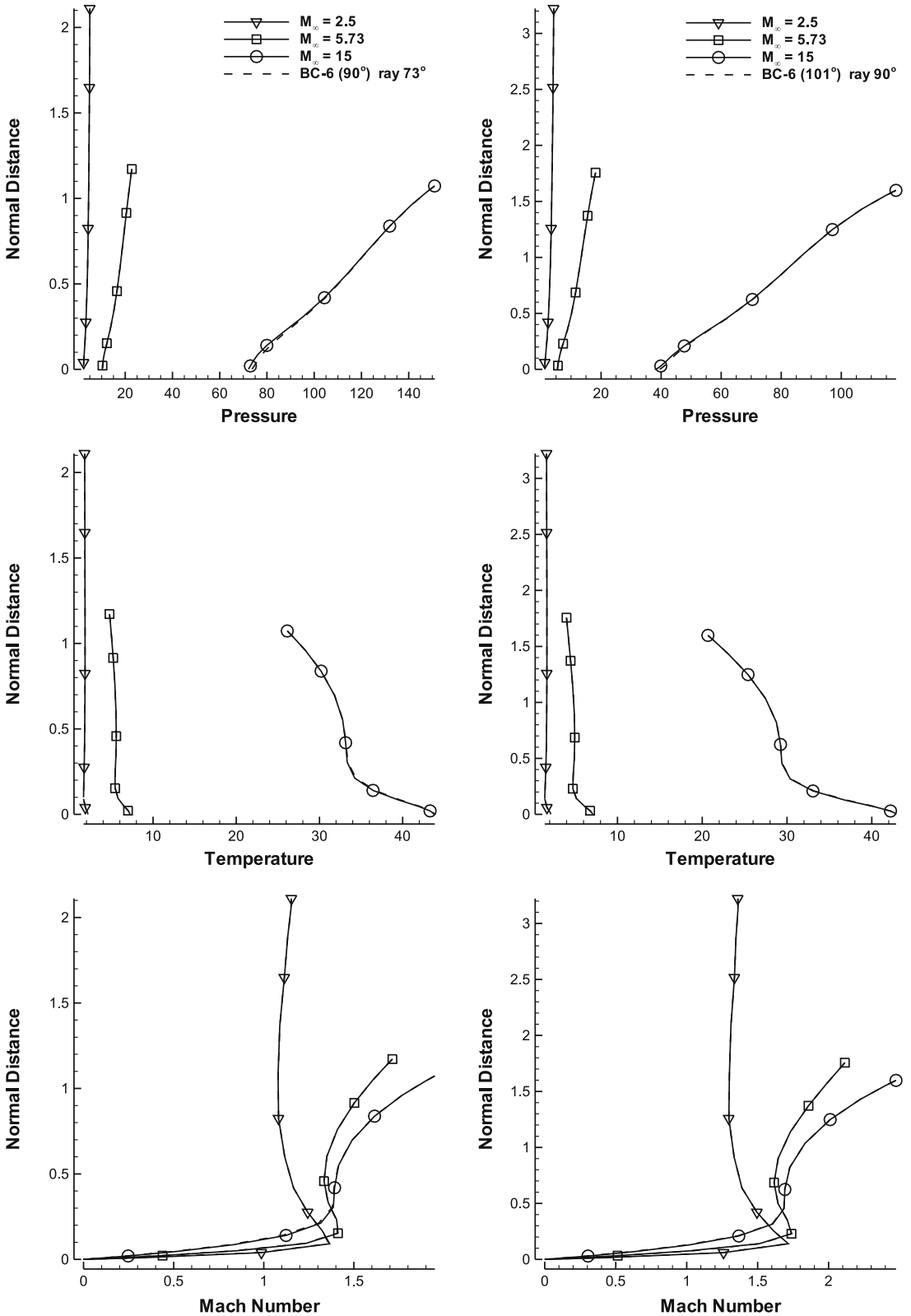

Fig. 24. Profiles of the flow variables across the outflow boundary of the adiabatic cylinder at $Re_\infty = 2050$ using **BC-6** for different Mach numbers and for two different arc lengths (73° left and 90° right). The dashed lines represent the values at internal counterpart from a large domain (90° for the left column and 101° for the right column).

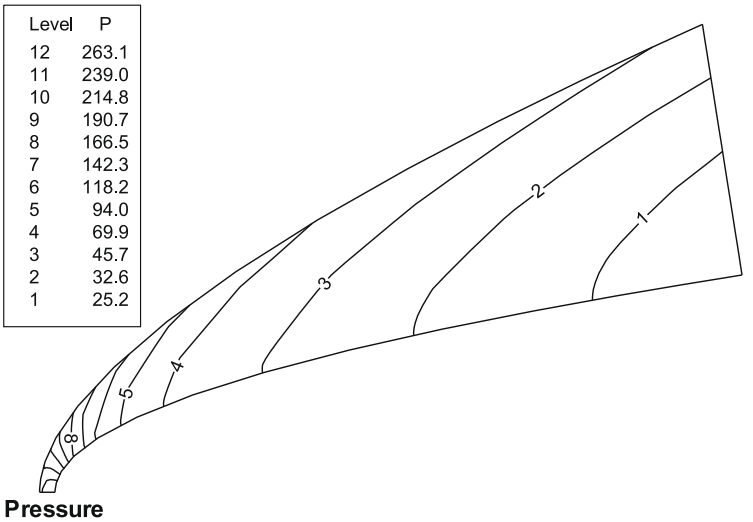
Level P
12 263.1
11 239.0
10 214.8
9 190.7
8 166.5
7 142.3
6 118.2
5 94.0
4 69.9
3 45.7
2 32.6
1 25.2
1
2
3
4
5
6
8

Pressure

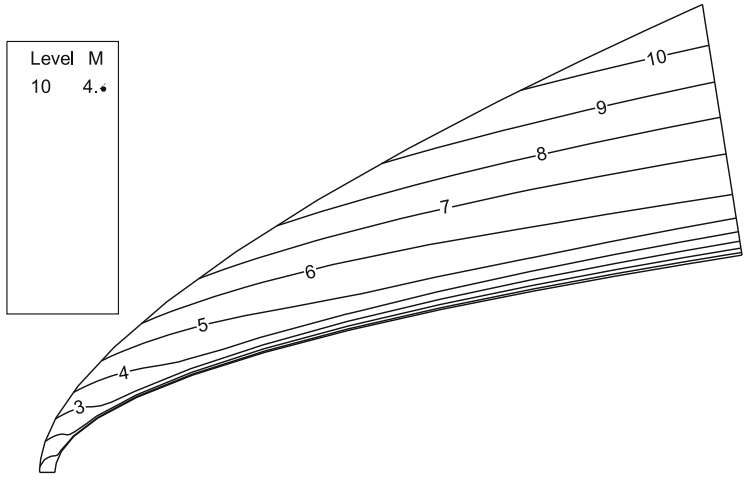
Level M
10 4.
10
9
8
7
6
5
4
3

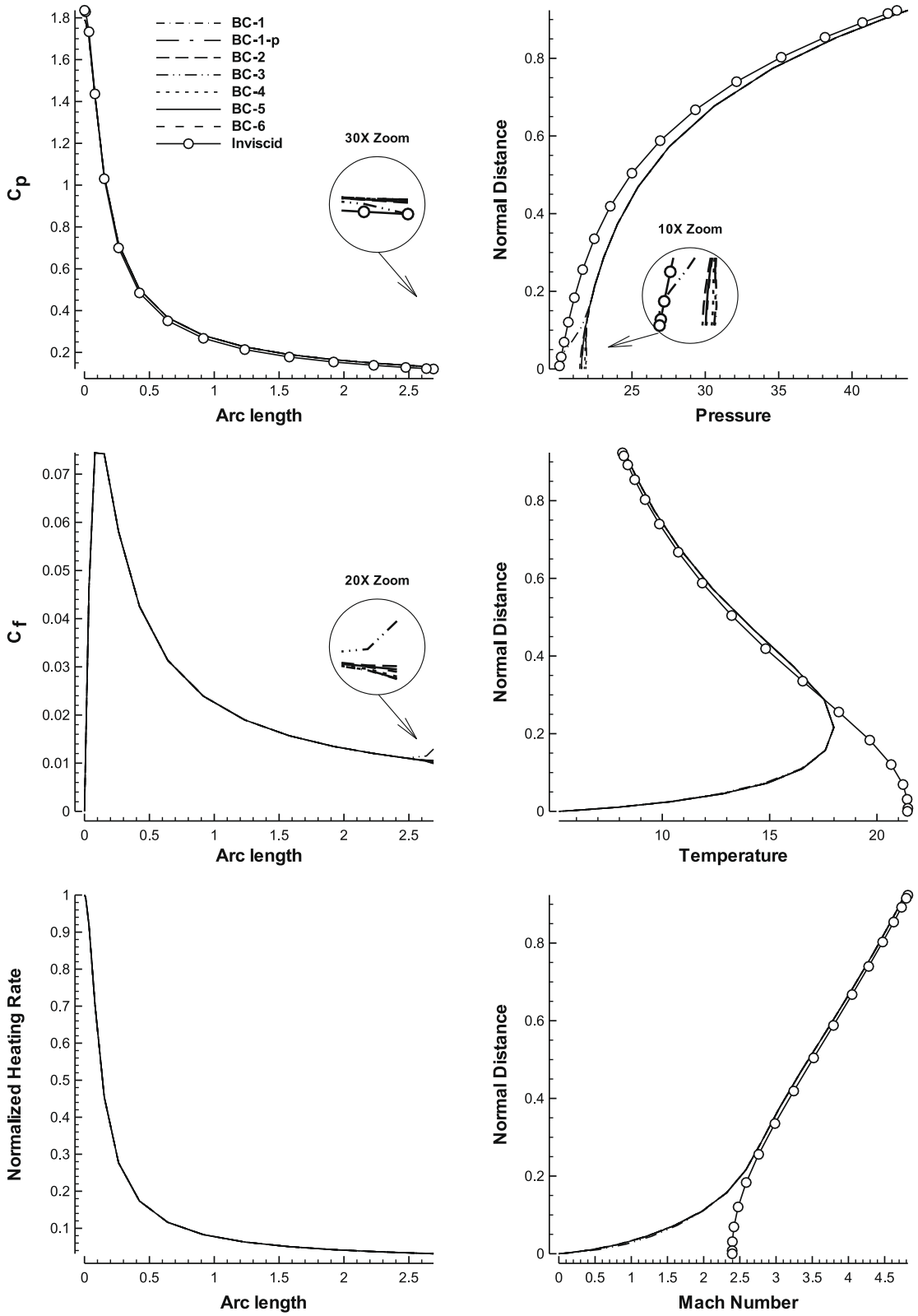

Fig. 26. Surface pressure coefficient, skin friction coefficient, surface heating rate normalized to the stagnation value (left column) and profiles of the flow variables across the outflow boundary (right column) for the isothermal parabola at $M_\infty = 15$ for different outflow conditions.

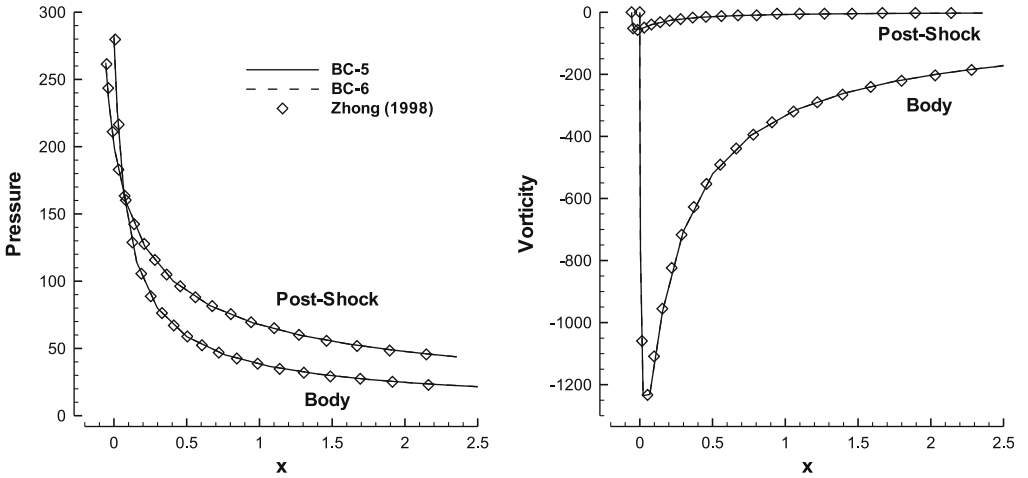

Fig. 27. Pressure and vorticity distributions on the body surface and just behind the bow shock for the isothermal parabola at $M_\infty = 15$ using **BC-5** and **BC-6**.

7. Conclusions

Different outflow boundary conditions have been studied and examined for numerical simulation of supersonic/hypersonic viscous flows over blunt bodies using spectral collocation methods. Detailed investigations have been carried out to examine the accuracy and performance of each outflow condition for two model geometries of different surface curvature variations to identify suitable subsonic outflow conditions for an accurate solution of the viscous blunt-body problem. Some conclusions regarding the present study are as follows:

(1) It is observed that although some external information (like, pressure) is only required for the subsonic portion of the outflow, it has a strong influence on the upper portion's flow field where the flow is supersonic within the boundary layer. It is also seen that the velocity and temperature normal gradients are considerably influenced in the boundary layer by the subsonic outflow pressure distribution.
(2) A verification procedure is suggested to identify the distinctive effect of each outflow condition by shrinking/extending the body geometry and the consequent computational domain. It is shown that inaccurate outflow boundary condition spoils the solution especially near the outflow. Therefore, accurate solution in the whole flow field needs suitable outflow boundary conditions to be implemented.
(3) It is found that the surface curvature plays an important role on how the subsonic outflow condition affects the surrounding flow field upstream of the outflow. This effect is more pronounced for the geometries with noticeable curvature near the outflow where high gradients of the flow variables occur.
(4) It is demonstrated that the extrapolation of all primitive variables through the subsonic region of the outflow (**BC-5**) and extrapolating only the pressure along with proper compatibility relations (**BC-6**) result in better and more accurate solutions than the others.
(5) A detailed accuracy analysis is performed for the different grid points and domain sizes for the proposed outflow boundary conditions, **BC-5** and **BC-6**. The study indicates that **BC-5** and **BC-6** have better performance than the others. When using computational domains of different size with a fixed grid size, the error in the smaller domain is less than the larger one. It confirms that for the spectral accuracy, one should increase the number of grid points when increasing the domain size.
(6) The accuracy and capability of the proposed outflow boundary conditions used are examined for different Reynolds and Mach number flows. It is demonstrated that for moderate Mach and Reynolds numbers, both **BC-5** and **BC-6** can provide accurate solutions. Comparing the obtained results using these two boundary conditions with other researcher's ones and experimental data shows good agreements and points out that they are quite accurate, efficient and self-stand in modeling the subsonic outflow boundary of the viscous blunt-body problem using spectral collocation schemes.

Acknowledgments

The authors would like to thank Sharif University of Technology and University of Tehran for financial support of this study. The authors also acknowledge the reviewers for their helpful suggestions, which have been incorporated in the final manuscript.

References

[1] S.V. Tsynkov, Numerical solution of problems on unbounded domains. A review, Appl. Numer. Math. 27 (4) (1998) 465–532.
[2] T. Colonius, Modeling artificial boundary conditions for compressible flow, Annu. Rev. Fluid Mech. 36 (2004) 315–345.
[3] J. Nordström, Accurate solutions of the Navier–Stokes equations despite unknown outflow boundary data, J. Comput. Phys. 120 (1) (1995) 184–205.
[4] J.P. Boyd, Chebyshev and Fourier Spectral Methods, second ed., Dover, New York, 2000.
[5] C. Canuto, M.Y. Hussaini, A. Quarteroni, T.A. Zang, Spectral Methods in Fluid Dynamics, Springer-Verlag, New York, 1987.
[6] D. Funaro, Polynomial Approximation of Differential Equations, Springer-Verlag, Berlin, Germany, 1992.
[7] D.A. Kopriva, T.A. Zang, M.Y. Hussaini, Spectral methods for the euler equations: the blunt body problem revisited, AIAA J. 29 (9) (1991) 1458–1462.
[8] M. Najafi, Spectral solution of flows with discontinuity, M.Sc. Dissertation, Amirkabir Univ. of Tech., Tehran, Iran, 2002.
[9] V. Esfahanian, M. Boroomand, M. Najafi, Spectral solution of high speed inviscid flows over cylinders and spheres, J. Fac. Eng. Tehran Univ. 40 (6) (2007) 789–802.
[10] K. Hejranfar, V. Esfahanian, M. Najafi, Spectral solution of high speed viscous flows over cylinders and spheres, in: Proceedings of the Sixth International Conference Iranian Aerospace Society (AERO2007), K.N. Toosi Univ. of Tech., Tehran, Iran, February 24–26, 2007.
[11] J.C. Strikwerda, Initial boundary value problems for incompletely parabolic systems, Commun. Pure Appl. Math. 33 (1977) 797–822.
[12] M.E. Hayder, E. Turkel, High order accurate solutions of viscous problems, AIAA Paper 93-3074, presented at the AIAA 24th Fluid Dynamics Conference, Orlando, FL, July 6–9, 1993.
[13] J. Oliger, A. Sundstrom, Theoretical and practical aspects of some initial boundary-value problems in fluid-dynamics, SIAM J. Appl. Math. 35 (3) (1978) 419–446.
[14] M.H. Carpenter, D. Gotlieb, S. Abarbanel, The stability of numerical boundary treatments for compact high-order finite difference schemes, J. Comput. Phys. 108 (2) (1993) 272–295.
[15] M.H. Carpenter, D. Gotlieb, S. Abarbanel, Stable and accurate boundary treatments for compact high-order finite-difference schemes, Appl. Numer. Math. 12 (1) (1993) 55–87.
[16] S. Abarbanel, A.E. Chertock, A. Yefet, Strict stability of high-order compact implicit finite-difference schemes: the role of boundary conditions for hyperbolic PDEs, I, J. Comput. Phys. 160 (1) (2000) 42–66.
[17] B. Gustafsson, H.-O. Kreiss, A. Sundstrom, Stability theory of difference approximation for mixed initial boundary value problems II, Math. Comput. 26 (119) (1972) 649–686.
[18] M.H. Carpenter, D. Gotlieb, S. Abarbanel, Time-stable boundary conditions for finite-difference schemes solving hyperbolic systems: methodology and application to high-order compact schemes, J. Comput. Phys. 111 (2) (1994) 220–236.
[19] K.W. Thompson, Time dependent boundary conditions for hyperbolic systems, J. Comput. Phys. 68 (1) (1987) 1–24.
[20] T.J. Poinsot, S.K. Lele, Boundary conditions for direct simulations of compressible viscous flows, J. Comput. Phys. 101 (1) (1992) 104–129.
[21] C. Hirsch, Numerical Computation of Internal and External Flows, vol. 2, John Wiley & Sons, New York, 1990.
[22] P. Dutt, Stable boundary conditions and difference schemes for Navier–Stokes equations, SIAM J. Numer. Anal. 25 (2) (1988) 245–267.
[23] T. Hagstrom, S.I. Hariharan, Accurate boundary conditions for exterior problems in gas dynamics, Math. Comput. 51 (158) (1988) 581–597.
[24] G.W. Hedstrom, Non-reflecting boundary conditions for nonlinear hyperbolic systems, J. Comput. Phys. 30 (1979) 222–237.
[25] J. Nordström, M. Svard, Well-posed boundary conditions for the Navier–Stokes equations, SIAM J. Numer. Anal. 43 (3) (2005) 231–1255.
[26] Y. Guo, N.A. Adams, L. Kleiser, Modeling of nonparallel effects in temporal direct numerical simulations of compressible boundary-layer transition, Theor. Comput. Fluid Dyn. 7 (1995) 141–157.
[27] C.D. Pruett, T.A. Zang, C.-L. Chang, M.H. Carpenter, Spatial direct numerical simulation of high-speed boundary-layer flows Part I: Algorithmic considerations and validation, Theor. Comput. Fluid Dyn. 7 (1995) 49–76.
[28] C.D. Pruett, C.-L. Chang, C.L. Streett, Simulation of crossflow instability on a supersonic highly swept wing, Comput. Fluids 29 (2000) 33–62.
[29] L. Kleiser, T.A. Zhang, Numerical simulation of transition in wall-bounded shear flows, Ann. Rev. Fluid Mech. 23 (1991) 495–537.
[30] X. Zhong, High-order finite-difference schemes for numerical simulation of hypersonic boundary-layer transition, J. Comput. Phys. 144 (2) (1998) 662–709.
[31] X. Zhong, Direct numerical simulation of hypersonic boundary-layer transition over blunt leading edges. I – A new numerical method and validation, AIAA Paper 97-0755, presented at the 35th AIAA Aerospace Sciences Meeting and Exhibit, Reno, NV, January 6–9, 1997.
[32] D.A. Kopriva, Spectral solution of the viscous blunt-body problem, AIAA J. 31 (7) (1993) 1235–1242.
[33] D.A. Kopriva, Spectral solution of the viscous blunt-body problem 2: multidomain approximation, AIAA J. 34 (3) (1996) 560–564.
[34] D.A. Kopriva, Shock-fitted multidomain solution of supersonic flows, Comput Methods Appl. Mech. Eng. 175 (1999) 383–394.
[35] A. Kumar, R.A. Graves, Numerical solution of the viscous hypersonic flow past blunted cones at angle of attack, AIAA Paper 77-172, 1977.
[36] B. Gustafsson, J. Nordström, Extrapolation procedures at outflow boundaries for the Navier–Stokes equations, in: Lichnewsky, Glowinski (Eds.), Computing Methods in Applied Sciences and Engineering, SIAM, Philadephia, PA, 1990, pp. 36–150.
[37] J. Nordström, Extrapolation procedures for the time-dependent Navier–Stokes equations, AIAA J. 30 (6) (1992) 1654–1656.
[38] J. Nordström, on flux-extrapolation at supersonic outflow boundaries, Appl. Numer. Math. 30 (1990) 447–457.
[39] Z.U.A. Warsi, Fluid Dynamics: Theoretical and Computational Approaches, CRC Press, Taylor & Francis Group, Boca Raton, 2006.
[40] G. Moretti, M.D. Salas, The blunt body problem for a viscous rarefied gas flow, AIAA Paper 69-139, January 1969.
[41] G.P. Brooks, J.M. Powers, A Karhunen–Loève least-squares technique for optimization of geometry of a blunt body in supersonic flow, J. Comput. Phys. 195 (1) (2004) 387–412.
[42] F.S. Billig, Shock-wave shapes around spherical and cylindrical nosed bodies, J. Spacecraft Rockets 4 (6) (1967) 822–823.
[43] G. Erlebacher, M.Y. Hussaini, Numerical experiments in supersonic boundary-layer stability, Phys. Fluids A 2 (1) (1990) 94–104.
[44] C.D. Pruett, T.A. Zang, Direct numerical simulation of laminar breakdown in high-speed, axisymmetric boundary layers, Theor. Comput. Fluid Dyn. 3 (6) (1992) 345–367.
[45] Y.C. Vigneron, J.V. Rakich, J.C. Tannehill, Calculation of supersonic viscous flow over delta wings with sharp subsonic leading edges, AIAA Paper 78-1137, presented at the 11th AIAA Fluid and Plasma Dynamics Conference, Seattle, Washington, July 10–12, 1978.
[46] S.G. Rubin, T.C. Lin, Numerical methods for two- and three-dimensional viscous flow problems: application to hypersonic leading edge equations, J. Comput. Phys. 9 (1972) 339–364.
[47] L.B. Schiff, J.L. Steger, Numerical simulation of steady supersonic viscous flow, AIAA J. 18 (12) (1980) 1421–1430.
[48] J.C. Tannehill, D.A. Anderson, R.H. Pletcher, Computational Fluid Mechanics and Heat Transfer, second ed., Taylor & Francis, Washington, DC, 1997.
[49] C.L. Streett, T.A. Zang, M.Y. Hussaini, Spectral methods for solution of the boundary-layer equations, AIAA Paper 84-0170, presented at the 22nd AIAA Aerospace Sciences Meeting, Reno, NV, January 9–12, 1984.
[50] Christopher J. Roy, Review of code and solution verification procedures for computational simulation, J. Comput. Phys. 205 (1) (2005) 131–156.
[51] V. Esfahanian, Computation and stability analysis of laminar flow over a blunt cone in hypersonic flow, Ph.D. Dissertation, The Ohio State University, 1991.
[52] P.A. Gnoffo, Complete supersonic flow fields over blunt bodies in a generalized orthogonal coordinate system, AIAA J. (6) (1980) 611–612.
[53] O.K. Tewfik, W.H. Giedt, Heat transfer, recovery factor and pressure distributions around a circular cylinder normal to a supersonic rarefied-air stream, J. Aero. Sci. 27 (10) (1960) 721–729.